NASA Technical Paper 1633

Investigation of the Flow Field Surrounding Circular-Arc Boattail Nozzles at Subsonic Speeds

William K. Abeyounis and Lawrence E. Putnam

MAY 1980

NASA

NASA Technical Paper 1633

Investigation of the Flow Field Surrounding Circular-Arc Boattail Nozzles at Subsonic Speeds

William K. Abeyounis and Lawrence E. Putnam
Langley Research Center
Hampton, Virginia

National Aeronautics
and Space Administration

**Scientific and Technical
Information Office**

1980

SUMMARY

An investigation has been conducted to determine the effects of jet exhuast on the subsonic flow surrounding two circular-arc boattail nozzles with attached and separated boundary layers. Measurements of local Mach numbers and flow angles were made at subsonic free-stream Mach numbers of 0.60 and 0.80 at an angle of attack of 0° in the Langley 16-Foot Transonic Tunnel. Jet-exhaust flow was simulated with a solid cylindrical sting and with high-pressure air at jet-nozzle total-pressure ratios of 2.9 and 5.0. Results show strong effects of the jet-wave structure on the external flow field. However, the shape of the jet-exhaust plume more than one exhaust wavelength downstream of the nozzle exit had little effect on the nozzle surface pressures. The predicted local Mach numbers and flow angles for attached-flow nozzles with solid jet simulators obtained by using subsonic inviscid/viscous-flow theory are in good agreement with experimental data. When jet-entrainment effects are included, predictions of the nozzle surface-pressure distributions also agree with experimental data for the attached-flow nozzles with high-pressure air jets.

INTRODUCTION

Current analytical predictions of the pressure distributions and drag for boattail-nozzle configurations for which boundary-layer separation occurs at subsonic speeds generally do not agree with experimental data. Most prediction techniques in use today combine an empirical model of the viscous flow in the separated region with a conventional boundary-layer solution and a solution for inviscid outer flow (refs. 1 to 6). These analytical methods typically represent the jet-exhaust plume as a solid body with the geometry determined by an inviscid-flow solution. As a result, the effects of entrainment of the external airstream by the jet-exhaust flow on the nozzle pressure distributions and drag are neglected. Experimental data (ref. 7) show that the drag of a nozzle with a cylindrical solid jet simulator is less than the drag of that nozzle with an air jet at the design nozzle pressure ratio (jet total pressure to free-stream static pressure) of 2. This difference is due primarily to entrainment effects. To obtain better predictions, improved analytical methods which include the jet-entrainment effects must be developed. In order to accomplish this, an improved understanding of the physics of the flow is required.

The purpose of this study was to gain an understanding of the flow field surrounding boattail-nozzle configurations at subsonic speeds, including the effects of the jet exhaust on the flow field, and to compare computed values with experimental results. Measurements were made of the surface pressures and of the local Mach numbers and flow angles in the flow surrounding a long circular-arc boattail nozzle with unseparated flow and a short circular-arc boattail nozzle with separated flow (ref. 8). Measurements of the pitot pressures in the jet and shear layer for these same two nozzles are presented in reference 9.

SYMBOLS

C_p pressure coefficient, $\frac{p - p_\infty}{q_\infty}$

D maximum model diameter, cm

d_b nozzle boattail-base diameter, cm

d_e nozzle-exit diameter, cm

l nozzle boattail length, cm

M Mach number

NPR jet-nozzle total-pressure ratio, $p_{t,j}/p_\infty$

p pressure, Pa

q dynamic pressure, Pa

R boattail circular-arc radius, cm

r radial distance from model centerline, cm

S nozzle-convergence length, cm (see fig. 2(b))

s axial coordinate in nozzle-convergence section, cm (see fig. 2(b))

t nozzle-throat length, cm (see fig. 2(b))

β terminal boattail angle, deg

β_c boattail chord angle, deg

ΔM difference between local Mach number and free-stream Mach number, $M - M_\infty$

Δx axial distance aft from start of boattail, cm

θ flow angle relative to free-stream velocity, positive upward, deg

Subscripts:

e exit

j jet

t total

1,2,3 probe total-pressure numbers (see fig. 3)

∞ free stream

EXPERIMENTAL APPARATUS AND PROCEDURE

Wind Tunnel

The investigation was conducted in the Langley 16-Foot Transonic Tunnel. The tunnel is a single-return, continuous-flow atmospheric tunnel. It has an octagonal test section with eight longitudinal slots and has continuous air exchange for cooling. The free-stream Mach number is continuously variable from 0 to 1.30. The average Reynolds number per meter varies from approximately 9.3×10^6 at $M_\infty = 0.20$ to approximately 12.6×10^6 at $M_\infty = 1.30$. A more detailed description of the Langley 16-Foot Transonic Tunnel can be found in reference 10.

Model and Support System

The experimental apparatus used in this investigation is shown in figure 1. An isolated, single-engine nacelle model was mounted in the tunnel on a sting-strut support system. The nose of the model was attached to the strut blade. The blade was swept 45° and was 5 percent thick with a 50.80-cm chord in the streamwise direction. The sting was 5.08 cm by 10.16 cm in cross section, with the top and bottom capped with half-cylinders of 2.54-cm radius. The centerline of the sting was 55.88 cm below the wind-tunnel centerline. This placed the model axis on the tunnel centerline, with the tip of the model nose at tunnel station 39.78 m. The model blockage was 0.099 percent of the test-section cross-sectional area, and the maximum blockage of the model and support system was 0.148 percent.

A sketch of the single-engine nacelle model is shown in figure 2(a). The external forebody shape consisted of an ogive nose followed by a straight cylindrical section. Two nozzle configurations were used in the investigation: a nozzle with $l/D = 0.80$ and $d_b/D = 0.51$, and a nozzle with $l/D = 1.768$ and $d_b/D = 0.51$. Boattails for the nozzles started at model station 137.16 cm. A more detailed description of the geometry of the nozzles is presented in figures 2(b) and 2(c).

The surface-pressure orifice locations are presented in table I. The interchangeable, convergent circular-arc boattail nozzles were attached at model station 127.00 cm. The jet was either powered with high-pressure air or simulated with a solid cylinder 27.94 cm long with a diameter equal to the nozzle-exit diameter. The solid cylinder simulated the jet-exhaust flow for a jet with a nozzle pressure ratio (jet total pressure to free-stream static pressure) of 2.

Flow Survey Mechanism, Probe, and Probe Calibration

A combination total-pressure probe was used in this investigation to determine the local Mach numbers and flow angles. Details of this probe are shown in figure 3. The probe was constructed out of three 0.0808-cm-diameter stainless-steel tubes. The tips of the two outer tubes were cut at an angle of 30° with respect to the probe centerline and the tip of the center tube was normal to the probe centerline.

The probe was positioned in the tunnel with the flow survey mechanism shown in figure 1. The probe was mounted at the end of a probe-support sting which was attached to the translating mechanism. The whole assembly was mounted on the strut head of the tunnel angle-of-attack strut. The survey mechanism has three degrees of freedom: axial translation, radial translation along the blade, and rotation of the blade. This provides the capability to survey anywhere in a cylinder with diameter of 122 cm, the axis of which corresponds to the tunnel centerline from tunnel station 40.69 m to station 41.91 m.

The difference in the pressures measured by the two outer orifices of the probe nondimensionalized by the local total pressure measured by the center orifice of the probe is approximately proportional to the local flow angle relative to the probe axis. The sum of the pressures measured by the two outer orifices nondimensionalized by the local total pressure is proportional to the local Mach number. The variation of these two parameters with Mach number and flow angle was determined by a calibration in the tunnel. Calibration tests were made at Mach numbers from 0.40 to 0.95 at angles of attack from approximately -10° to 10°. Upright and inverted tests were made in order to account for tunnel flow misalignment. The results of this calibration are shown in figure 3. (Note that calibration data points were obtained at increments of 1°; however, for clarity, only data at increments of 3° are shown.) The measured pressures obtained during the investigation were reduced to local Mach numbers and flow angles by using a double interpolation scheme.

Instrumentation

Pressure measurements were made with individual, remotely located electrical strain-gage pressure transducers. All pressure transducers were calibrated to an accuracy of ±0.5 percent of the capacity of the gage. For probe total-pressure gages and for model-surface static-pressure gages, the values were 17.2 and 34.5 kPa; for jet total-pressure gages, the value was 689 kPa.

Position measurements of the flow survey probe were made with helipots calibrated to an accuracy of ±0.25 percent of the helipot range. Translation measurements were made with 100-turn helipots; rotational measurements were made with 10-turn helipots. The resulting accuracy of the measurements (including a slight angular misalignment between the model and translating-mechanism axes) was approximately ±0.15 cm, or ±0.01 model diameter, for linear measurements and ±0.5° for angular measurements.

Tests

This investigation was made at free-stream Mach numbers of 0.60 and 0.80 with the model at an angle of attack of 0^{o}. Tests were made with each nozzle with the jet off ($p_{t,j}/p_{\infty} \approx 1.0$) and with the jet operating at ratios of jet total pressure to free-stream static pressure of 2.9 and 5.0. Tests were also made with the solid simulator attached to each nozzle. By use of the criteria described in references 11 and 12, boundary-layer transition was fixed with a 0.254-cm strip of No. 100 grit located 2.54 cm from the tip of the nose. Longitudinal surveys of the flow surrounding the various nozzle configurations were made at radial locations of approximately 0.25, 0.37, 0.62, 0.75, 1.00, and 1.50 model diameters from the model centerline. These longitudinal surveys were made at discrete points from 0.4 model diameter upstream of the start of the boattail to around 2.2 model diameters downstream of the nozzle exit. All the flow surveys were made in the vertical plane passing through the model centerline on the opposite side of the model from the sting strut in order to minimize support interference effects on the measurements.

THEORETICAL METHODS

Two analytical methods were used to predict surface-pressure distributions and local Mach numbers and flow angles in the flow field for comparison with experimental results. One method is a computer algorithm called DONBOL (ref. 13). DONBOL consists of a Neumann solution, with the Labrujere compressibility correction for the inviscid external flow, coupled with a modified Reshotko-Tucker integral boundary-layer technique, the control-volume method of Presz for calculating flow in the separated region, and an inviscid one-dimensional solution for the jet-exhaust flow. The viscous and inviscid flows are solved iteratively until convergence is obtained. The effects of jet-plume entrainment are neglected, the result of which is that jet-exhaust flows are treated as solid bodies. This method is limited to subsonic free-stream Mach numbers less than that Mach number for which the flow over the body first becomes sonic.

The other method used in this comparative study is the method of Wilmoth (ref. 14). This viscous-inviscid interaction method accounts for jet-entrainment effects in the prediction of subsonic flow over nozzle afterbodies. RAXBOD, the portion of this method which applies to inviscid flow, is the relaxation procedure of South and Jameson for the full-potential transonic-flow equation (ref. 15). The inviscid code is coupled with a modified Reshotko-Tucker integral boundary-layer technique (ref. 16), an inviscid jet code (ref. 17), and a jet-entrainment code (ref. 18). The jet-entrainment model is based on the concept of a weakly interacting shear layer in which the local streamline deflections due to entrainment are accounted for by a displacement-thickness type correction to the inviscid plume boundary. The plume boundary is calculated for one wavelength of the jet shock-wave pattern and then set to a constant value out to infinity. This method can be used for free-stream Mach numbers extending up into the transonic regime.

RESULTS AND DISCUSSION

Presentation of Results

Surface-pressure distributions and flow-field data were obtained at free-stream Mach numbers of 0.60 and 0.80 at an angle of attack of 0° for a circular-arc nozzle with $l/D = 0.80$ and $d_b/D = 0.51$ and for a circular-arc nozzle with $l/D = 1.768$ and $d_b/D = 0.51$. Measurements were made for the two nozzles with both solid simulators and high-pressure air to simulate jet exhausts. The surface-pressure distributions are presented in figures 4 to 7. Flow-field data corresponding to these conditions are presented in figures 8 to 21. Theoretical predictions from the two analytical methods are also presented in figures 4 to 21 for selected cases. The method of reference 13 is used to predict all cases except the jet-off cases. The method of reference 14 is used to predict all unseparated-flow cases except the jet-off case. The predictions from both methods in general agree well with experimental data. However, there are some regions where the predictions and the experimental data differ significantly.

Analysis of Experimental and Theoretical Differences

Probe.- Some of the differences between predicted and experimental data are probably due to experimental error. There were two sources of error in the flow-field data. One of these, the finite size of the probe, caused errors in several ways. Flow-angle and Mach number variations across the tip of the probe introduced errors into the point measurements. Total-pressure gradients in viscous regions such as the boundary layer and the jet-shear layer also caused errors. Also, as measurements were taken closer to the model surface, probe-model interference effects would be expected.

The other error source was a minor angular misalignment between the model and the probe axes. In addition, the probe was accidently bent before the data in figure 20 was taken, introducing a systematic error into the flow-angle data (but not the Mach number data) for this figure only. Comparison of the flow-angle data and theoretical predictions in figure 20(b) with similar flow-angle data and predictions in other figures indicates that the probe was probably bent between a half and one degree. (The flow angles just upstream of the boattail at $r/D = 1.50$ should be about the same for a given configuration.) Although the absolute magnitude of the flow-angle data of figure 20(b) is in error relative to the model, the changes in flow angle between data points are correct.

Theoretical viscous-region model.- Some of the differences between predicted values and experimental data within viscous regions are probably due also to the inadequacies of the theoretical methods. Both theoretical methods account for viscous effects on the external flow by calculating the inviscid flow over a modified body which consists of the geometrical body with a boundary-layer displacement thickness added. As shown in figures 8 and 9, good predictions for the external flow can be obtained in this way. However, within the viscous-flow region, the theoretical methods still treat the flow as an inviscid flow over the modified body. This causes the theoretical methods to

overpredict the local Mach numbers within the viscous region. This is particularly true for separated boundary-layer cases, as shown in figures 14 and 15, when comparisons are made deep inside a thick, complex three-dimensional viscous layer.

Theoretical jet model.- Simplifications in modeling the solid simulator and the high-pressure air jet led to some differences between predicted values and experimental data aft of the nozzle exit. Typical differences near the end of the solid simulator are shown in figures 4, 8, and 9. These differences occur because the body input into the computer codes extended farther downstream than did the actual solid simulator. Physically the local Mach number and flow-angle changes are caused by the flow expanding into the base flow region of the plume simulator. Typical differences for jet-on cases are shown in figures 11 to 13. Here the differences in the predictions of the two methods aft of the nozzle exit are partly due to differences in computing the inviscid plume shapes. Oscillations of the local Mach numbers and flow angles in the flow field surrounding the jet plume are not predicted by either of these theoretical methods. This is because the method of reference 13 uses only a one-dimensional inviscid jet-plume calculation with no jet-entrainment model, and the method of Wilmoth (ref. 14) assumes the plume shape is cylindrical after the first jet cellular shape. The predictions agree best with the data at the lower nozzle pressure ratios. It should be noted that the oscillations dampen rapidly in the external flow field and have little effect on the surface-pressure distributions. Because of the small effect of the oscillations on the boattail surface pressures, no effort was made to improve the flow-field calculations by incorporating a more sophisticated jet calculation.

Analysis of Differences in Analytic Methods

The main differences between the two analytic methods are that the method of Wilmoth (ref. 14) accounts for jet entrainment and the first jet cellular shape and that it solves the full-potential flow equation. Since the cases in which solid simulators were used had no jet entrainment, the differences in the predictions of the two methods for these cases would result solely from one method solving the full-potential flow equation. Except at transonic speeds, these differences should be negligible and the predictions should agree with experimental data. This is shown in figures 4, 8, and 9. The predictions of the two methods agree almost exactly with each other and with experimental data. In figure 4, the predictions differ most at the junction between the boattail and the solid simulator. These differences, however, are probably because the body geometry was input into the two computer programs differently. The input into the DONBOL computer program did not place a calculation point exactly at the boattail-solid simulator junction and caused the pressure peak there to be rounded off.

For jet-on cases, the effect of jet entrainment becomes important because it tends to increase the local velocities over the nozzle boattail. As shown in figure 5, the effect of jet entrainment must be accounted for in order to accurately predict surface-pressure distributions. The method of Wilmoth (ref. 14) does an excellent job of predicting the pressure distributions for the cases shown in the figure. Since for the solid-simulator case the

predictions of the two theoretical methods agree, the difference between the predictions for the jet-on case is an estimate of the magnitude of the jet-entrainment effect.

CONCLUSIONS

An investigation to determine the effect of the ratio of jet-total pressure to free-stream static pressure and the effect of the free-stream Mach number on the flow field surrounding two circular-arc boattail nozzles has been made. The test was conducted at subsonic speeds at an angle of attack of 0° in the Langley 16-Foot Transonic Tunnel. Theoretical predictions have been compared with the experimental results to ascertain the capabilities and deficiencies of current prediction methods. The results of the study indicate the following:

1. The jet exhaust has strong effects on the flow field near the nozzle. Especially evident was the influence of the wave structure of the jet plume on the external flow.

2. The shape of the jet-exhaust plume more than two exit diameters, or one exhaust wavelength downstream, of the nozzle exit appears to have little effect on the nozzle surface pressures.

3. The external flow field and the surface pressures can be adequately predicted with current methods for attached-flow nozzle boattails with solid jet simulators. Predictions for separated-flow nozzle boattails are less accurate because of the extent and greater complexity of the viscous layer.

4. The external flow field and the surface pressures can be adequately predicted about attached-flow nozzle boattails with high-pressure air jet exhaust when the effects of jet-plume entrainment and jet-plume growth are included.

Langley Research Center
National Aeronautics and Space Administration
Hampton, VA 23665
February 25, 1980

REFERENCES

1. Reubush, David E.; and Putnam, Lawrence E.: An Experimental and Analytical Investigation of the Effect on Isolated Boattail Drag of Varying Reynolds Number up to 130×10^6. NASA TN D-8210, 1976.

2. Rom, Josef; and Bober, Lawrence J.: Calculation of the Pressure Distribution on Axisymmetric Boattails Including Effects of Viscous Interactions and Exhaust Jets in Subsonic Flow. NASA TM X-3109, 1974.

3. Chow, Wen L.; Bober, Lawrence J.; and Anderson, Bernhard H.: Numerical Calculation of Transonic Boattail Flow. NASA TN D-7984, 1975.

4. Calarese, Wladimiro: Analysis of Transonic Viscous-Inviscid Interactions of Axisymmetric Afterbodies With Jet Effects and Boattail Injection in Separated Regions. AFFDL-TR-75-117, U.S. Air Force, Oct. 1975.

5. Presz, Walter M., Jr.; and Pitkins, Edward T.: An Analytical Model of Axisymmetric Afterbody Flow Separation. AIAA Paper No. 75-65, Jan. 1975.

6. Grossman, B.; and Melnik, R. E.: The Numerical Computation of the Transonic Flow Over Afterbodies Including the Effect of Jet-Plume and Viscous Interactions. AIAA Paper 75-62, Jan. 1975.

7. Reubush, David E.: Experimental Study of the Effectiveness of Cylindrical Plume Simulators for Predicting Jet-On Boattail Drag at Mach Numbers Up to 1.30. NASA TN D-7795, 1974.

8. Abeyounis, William Kelly: Boundary-Layer Separation on Isolated Boattail Nozzles. NASA TP-1226, 1978.

9. Mason, Mary L.; and Putnam, Lawrence E.: Pitot Pressure Measurements in Flow Fields Behind Circular-Arc Nozzles With Exhaust Jets at Subsonic Free-Stream Mach Numbers. NASA TM-80169, 1979.

10. Corson, Blake W., Jr.; Runckel, Jack F.; and Igoe, William B.: Calibration of the Langley 16-Foot Transonic Tunnel With Test Section Air Removal. NASA TR R-423, 1974.

11. Braslow, Albert L.; and Knox, Eugene C.: Simplified Method for Determination of Critical Height of Distributed Roughness Particles for Boundary-Layer Transition at Mach Numbers From 0 to 5. NACA TN 4363, 1958.

12. Braslow, Albert L.; Hicks, Raymond M.; and Harris, Roy V., Jr.: Use of Grit-Type Boundary-Layer-Transition Trips on Wind-Tunnel Models. NASA TN D-3579, 1966.

13. Putnam, Lawrence E.: DONBOL: A Computer Program for Predicting Axisymmetric Nozzle Afterbody Pressure Distributions and Drag at High Subsonic Speeds. NASA TM-78779, 1979.

14. Wilmoth, R. G.; Dash, S. M.; and Pergament, H. S.: A Numerical Study of Jet Entrainment Effects on the Subsonic Flow Over Nozzle Afterbodies. AIAA Paper 79-0135, Jan. 1979.

15. South, Jerry C., Jr.; and Jameson, Anthony: Relaxation Solutions for Inviscid Axisymmetric Transonic Flow Over Blunt or Pointed Bodies. AIAA Computational Fluid Dynamics Conference, July 1973, pp. 8-17.

16. Wilmoth, Richard G.: Computation of Transonic Boattail Flow With Separation. NASA TP-1070, 1977.

17. Dash, S. M.; and Thorpe, R. D.: A New Shock-Capturing/Shock-Fitting Computational Model for Analyzing Supersonic Inviscid Flows (The SCIPPY Code). Rep. No. 366, Aeronut. Res. Assoc. Princeton, Inc., Nov. 1978.

18. Dash, Sanford M.; and Pergament, Harold S.: A Computational Model for the Prediction of Jet Entrainment in the Vicinity of Nozzle Boattails (The BOAT Code). NASA CR-3075, 1978.

TABLE I.- PRESSURE-ORIFICE LOCATIONS ON NOZZLE BOATTAIL AND SOLID-SIMULATOR SURFACES

Pressure-orifice locations ($\Delta x/D$) for -			
Configuration 1 ($l/D = 0.80$; $d_b/D = 0.51$)		Configuration 2 ($l/D = 1.768$; $d_b/D = 0.51$)	
Boattail surface	Simulator surface	Boattail surface	Simulator surface
0.006	0.883	0.006	1.851
.052	.967	.105	1.935
.120	1.050	.239	2.018
.179	1.133	.377	2.101
.253	1.217	.504	2.185
.306	1.300	.654	2.268
.354	1.383	.765	2.351
.398	1.467	.851	2.435
.433	1.550	.939	2.518
.474	1.633	1.018	2.601
.503	1.717	1.088	2.685
.541	1.800	1.169	2.768
.570	1.967	1.230	2.935
.604	2.133	1.309	3.101
.665	2.300	1.371	3.268
.723	2.467	1.445	3.435
.782		1.503	
		1.580	
		1.638	
		1.720	

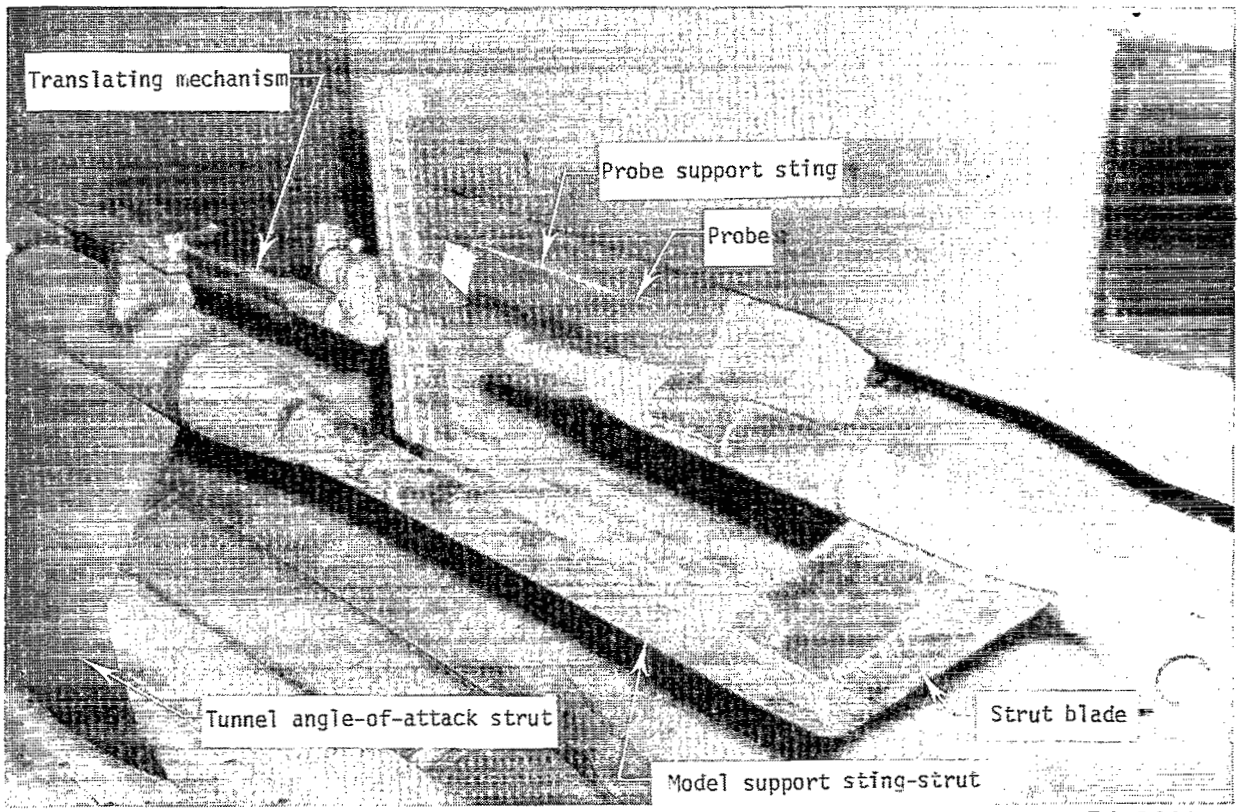

L-76-1298.2

Figure 1.- Experimental apparatus.

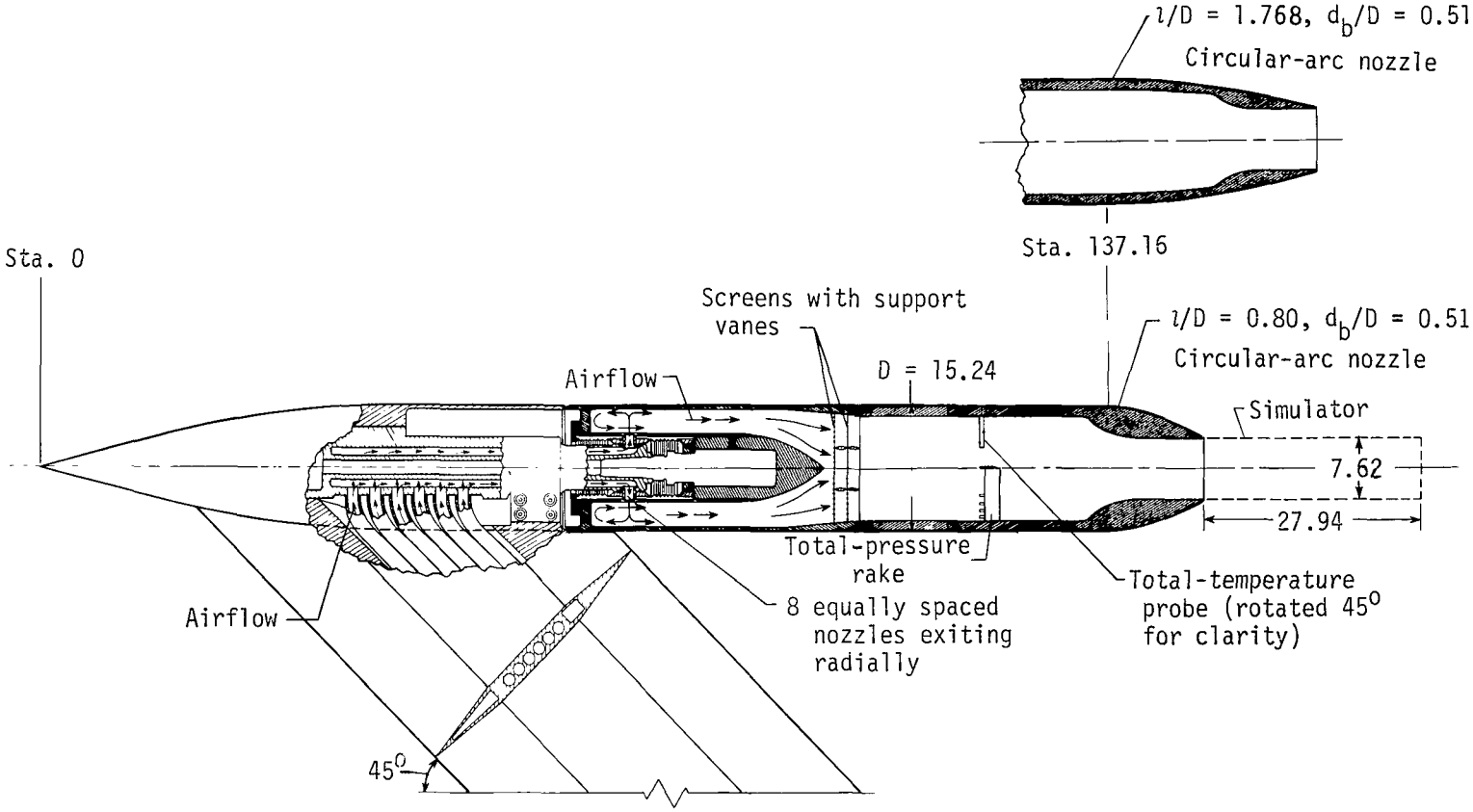

(a) Air-powered cone-cylinder model.

Figure 2.- Sketch of air-powered cone-cylinder model with details of nozzles and simulators. All dimensions are in centimeters unless otherwise noted.

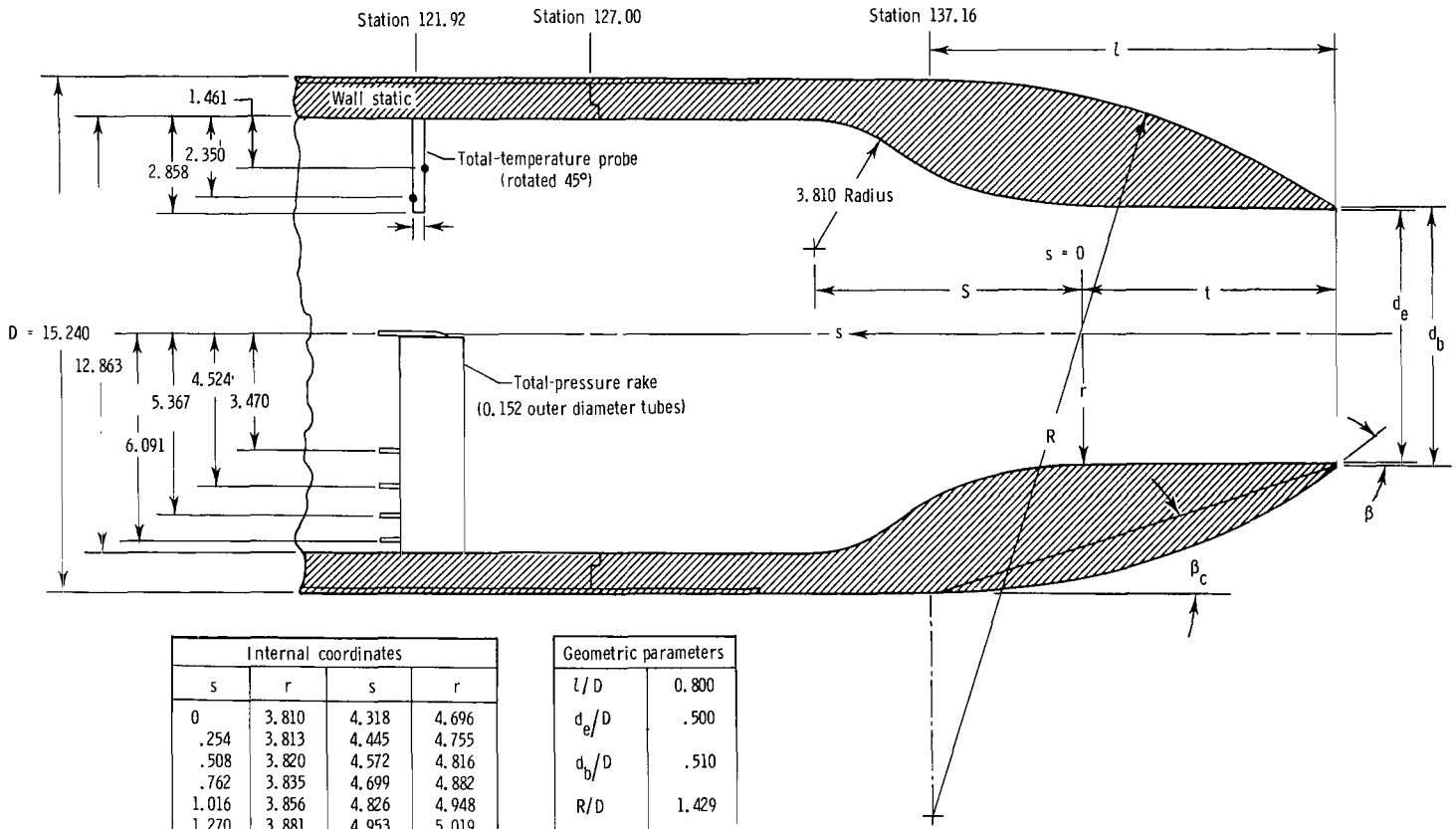

Internal coordinates			
s	r	s	r
0	3.810	4.318	4.696
.254	3.813	4.445	4.755
.508	3.820	4.572	4.816
.762	3.835	4.699	4.882
1.016	3.856	4.826	4.948
1.270	3.881	4.953	5.019
1.524	3.912	5.080	5.090
1.778	3.950	5.207	5.169
2.032	3.993	5.334	5.248
2.286	4.041	5.461	5.334
2.540	4.097	5.588	5.420
2.794	4.161	5.715	5.514
3.048	4.229	5.842	5.611
3.302	4.308	5.969	5.715
3.555	4.392	6.096	5.822
3.810	4.483	6.223	5.939
3.937	4.534	6.350	6.060
4.064	4.585	6.477	6.190
4.191	4.641		

Geometric parameters	
l/D	0.800
d_e/D	.500
d_b/D	.510
R/D	1.429
t/D	.500
S/D	.533
β, deg	34.054
β_c, deg	17.027

(b) Configuration 1.

Figure 2.- Continued.

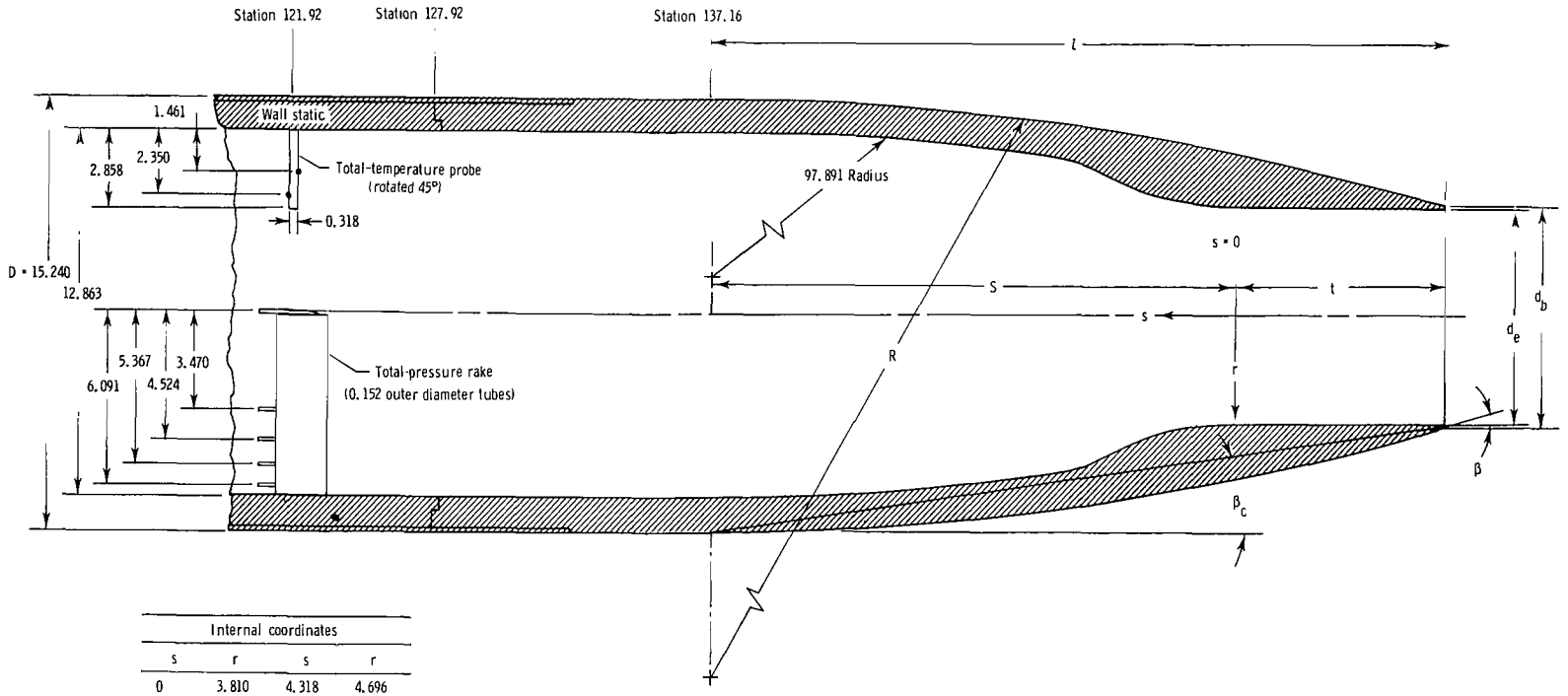

Internal coordinates			
s	r	s	r
0	3.810	4.318	4.696
.254	3.813	4.445	4.755
.508	3.820	4.572	4.816
.762	3.835	4.699	4.882
1.016	3.856	4.826	4.948
1.270	3.881	4.953	5.019
1.524	3.912	5.080	5.090
1.778	3.950	5.207	5.169
2.032	3.993	5.334	5.232
2.286	4.041	5.461	5.283
2.540	4.097	5.588	5.347
2.794	4.161	5.715	5.398
3.048	4.229	5.842	5.436
3.302	4.308	5.969	5.486
3.556	4.392	6.096	5.512
3.810	4.483	6.350	5.563
3.937	4.534	6.604	5.588
4.064	4.585	6.858	5.613
4.191	4.641	6.985	5.629

Geometric parameters	
l/D	1.768
d_e/D	.500
d_b/D	.510
R/D	6.500
t/D	.500
s/D	1.268
β, deg	15.781
β_c, deg	7.891

(c) Configuration 2.

Figure 2.- Concluded.

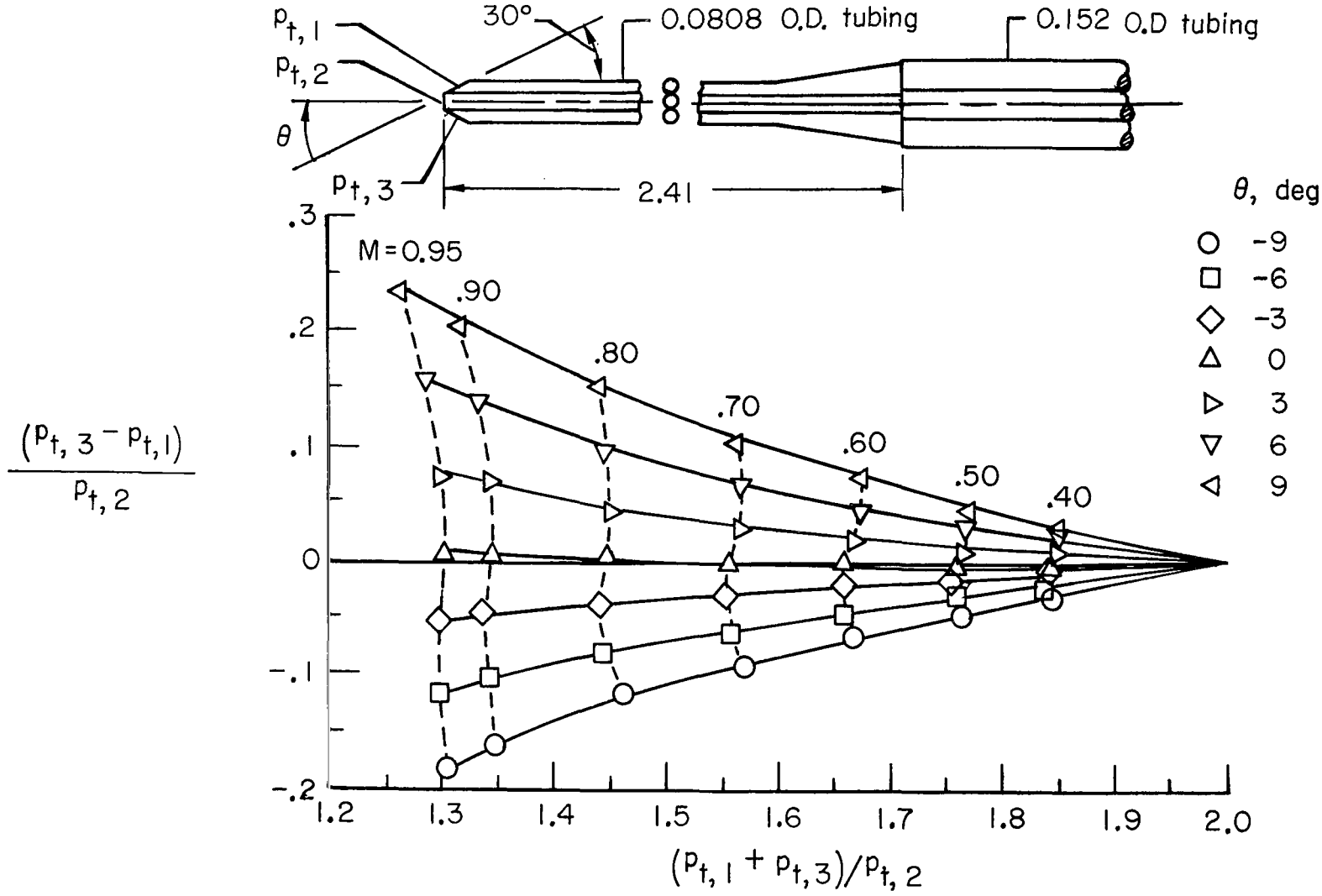

Figure 3.- Probe details and calibration.

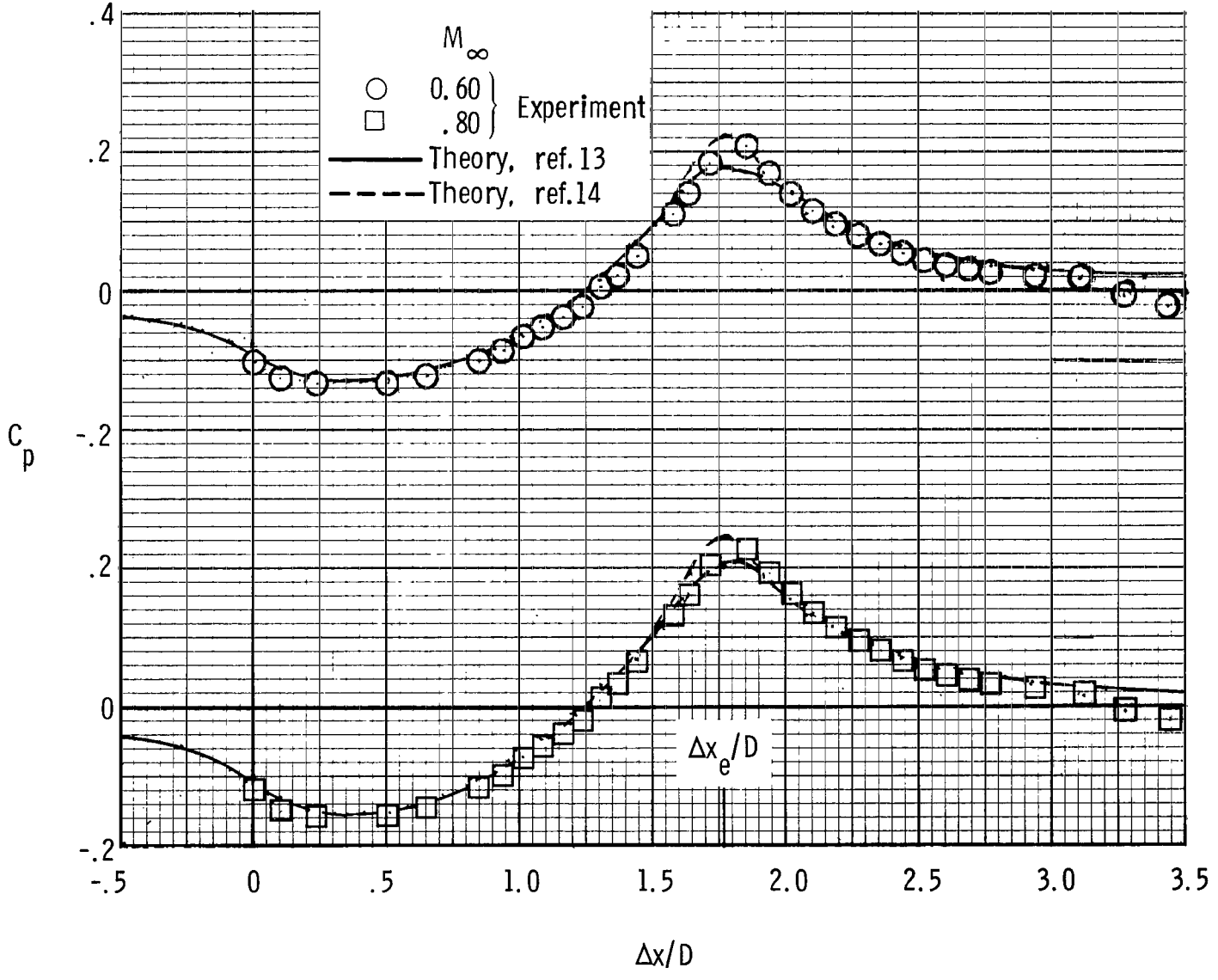

Figure 4.- Surface-pressure distributions for $\ell/D = 1.768$ nozzle with solid plume simulator.

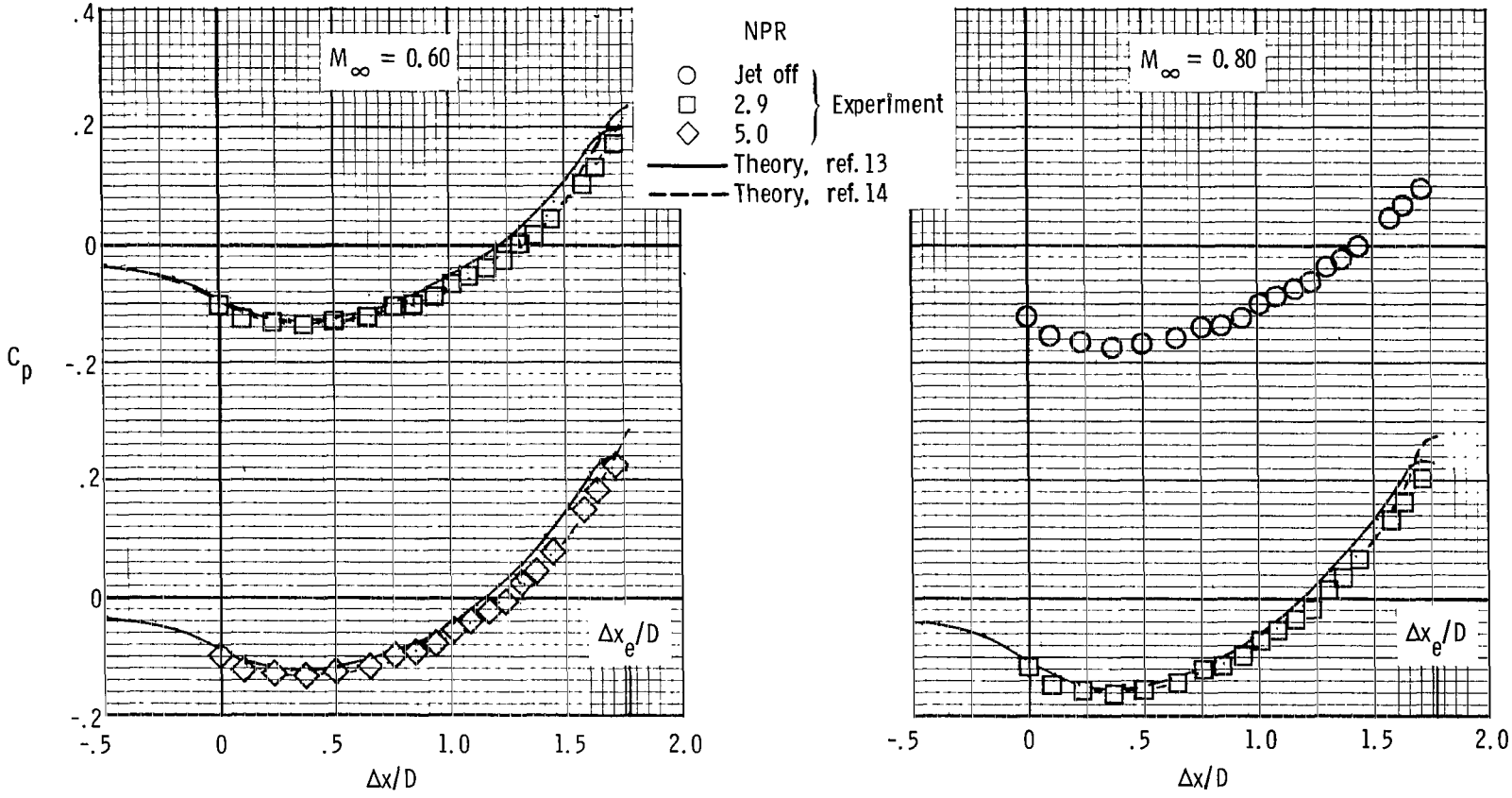

Figure 5.- Surface-pressure distributions for ℓ/D = 1.768 nozzle at various ratios of jet-total pressure to free-stream static pressure.

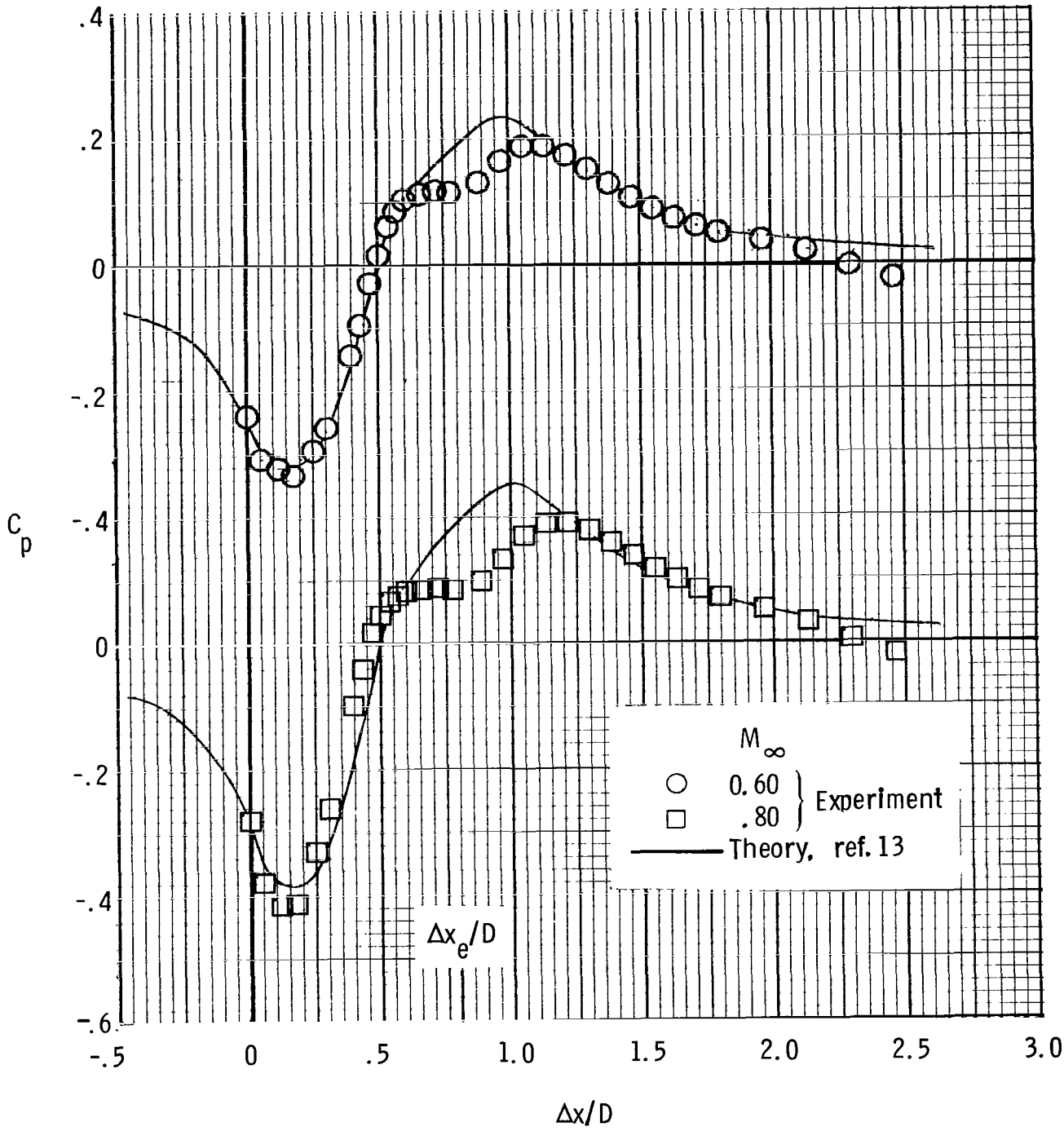

Figure 6.- Surface-pressure distributions for $\ell/D = 0.80$ nozzle with solid plume simulator.

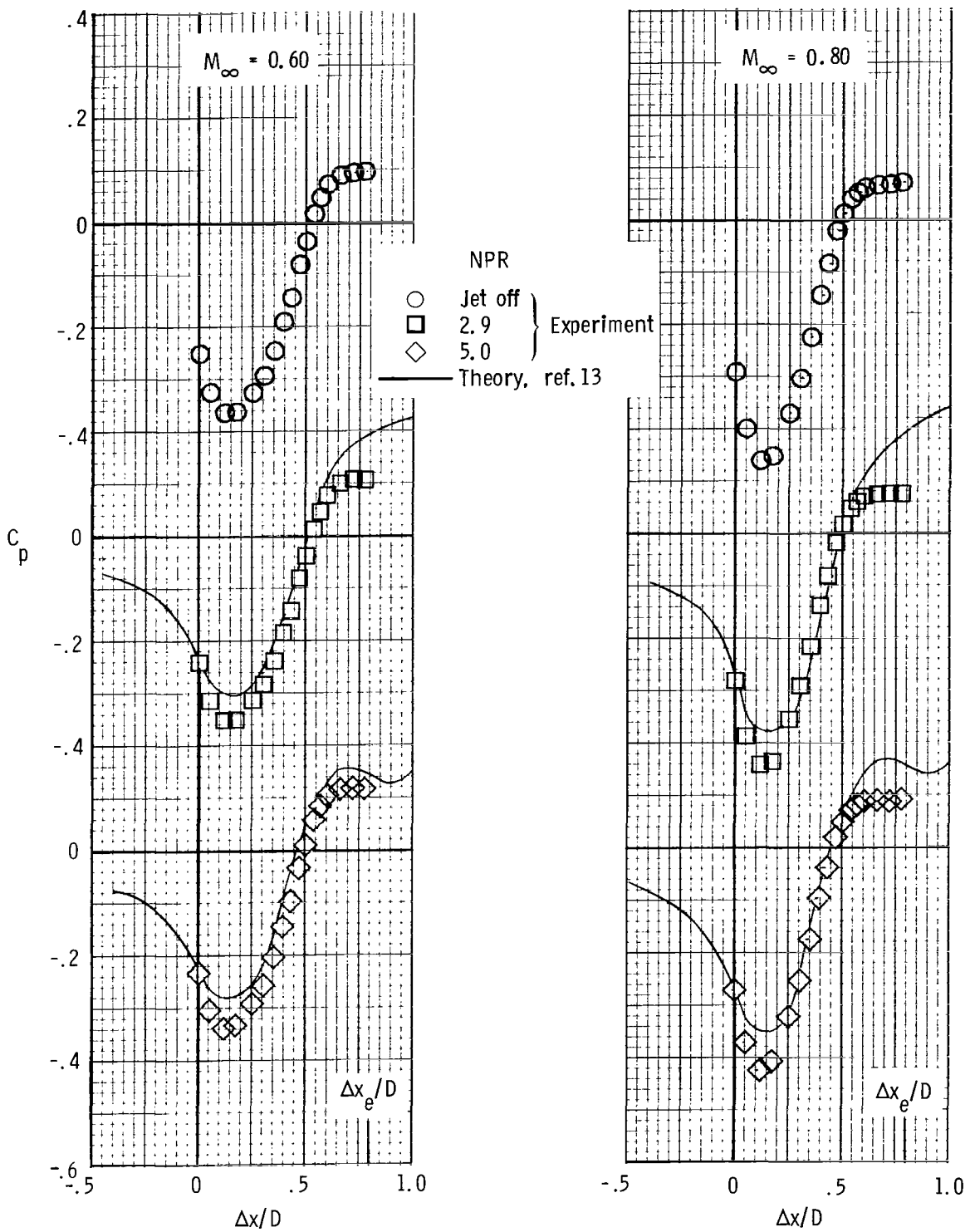

Figure 7.- Surface-pressure distributions for ℓ/D = 0.80 nozzle at various ratios of jet-total pressure to free-stream static pressure.

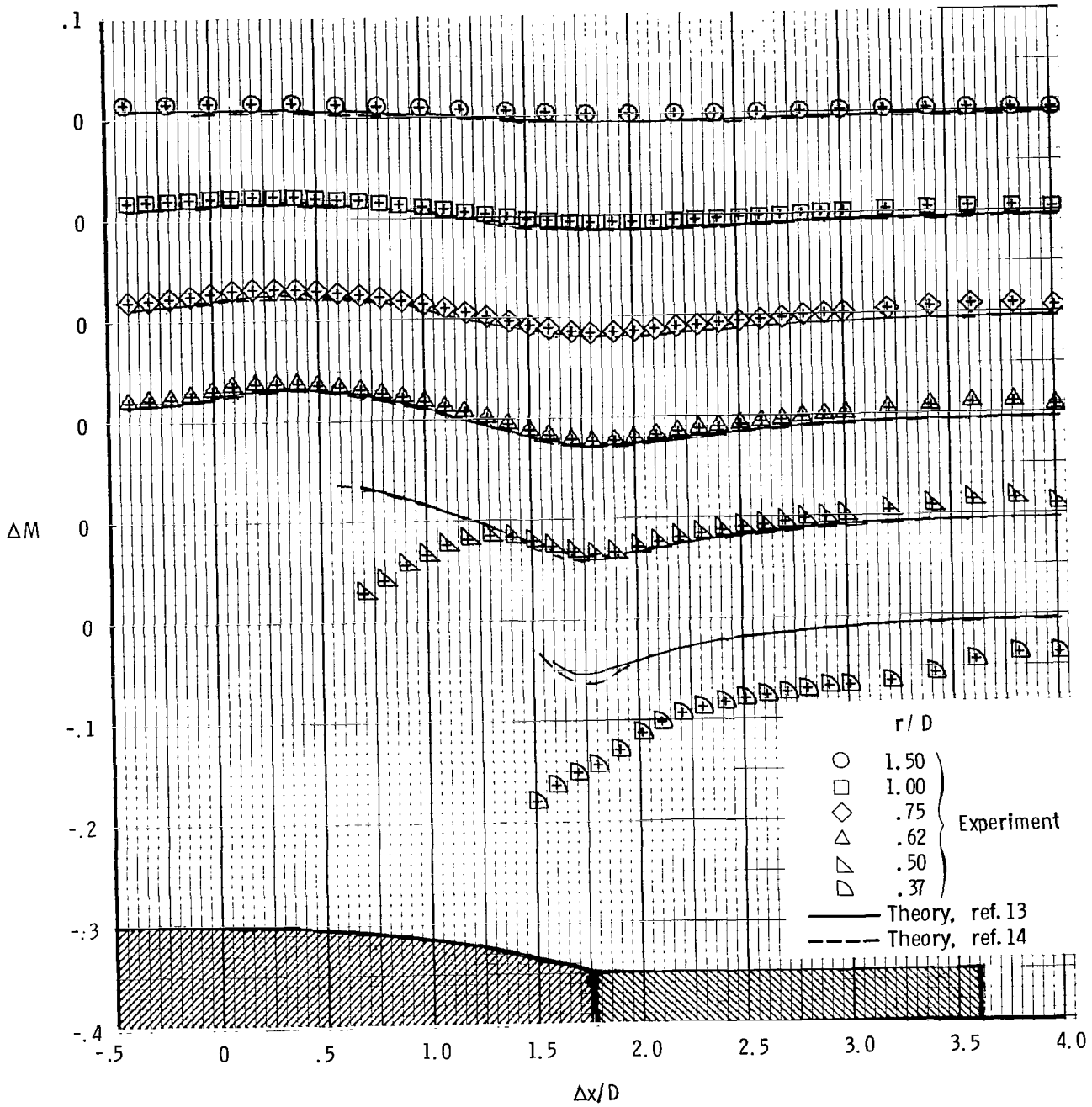

(a) Mach number.

Figure 8.- Flow-field characteristics for $l/D = 1.768$ nozzle with solid plume simulator at $M_\infty = 0.60$.

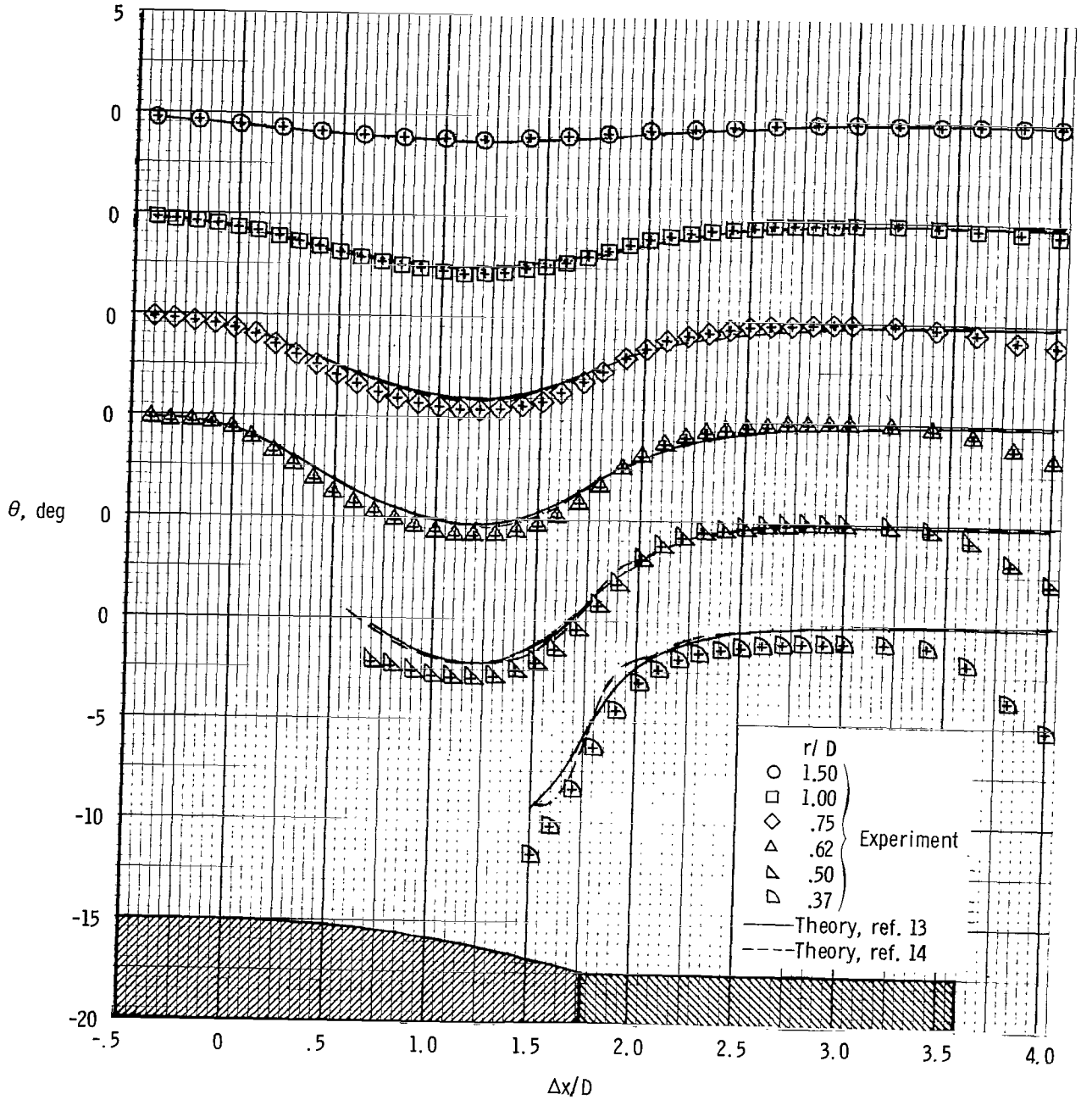

(b) Flow angle.

Figure 8.- Concluded.

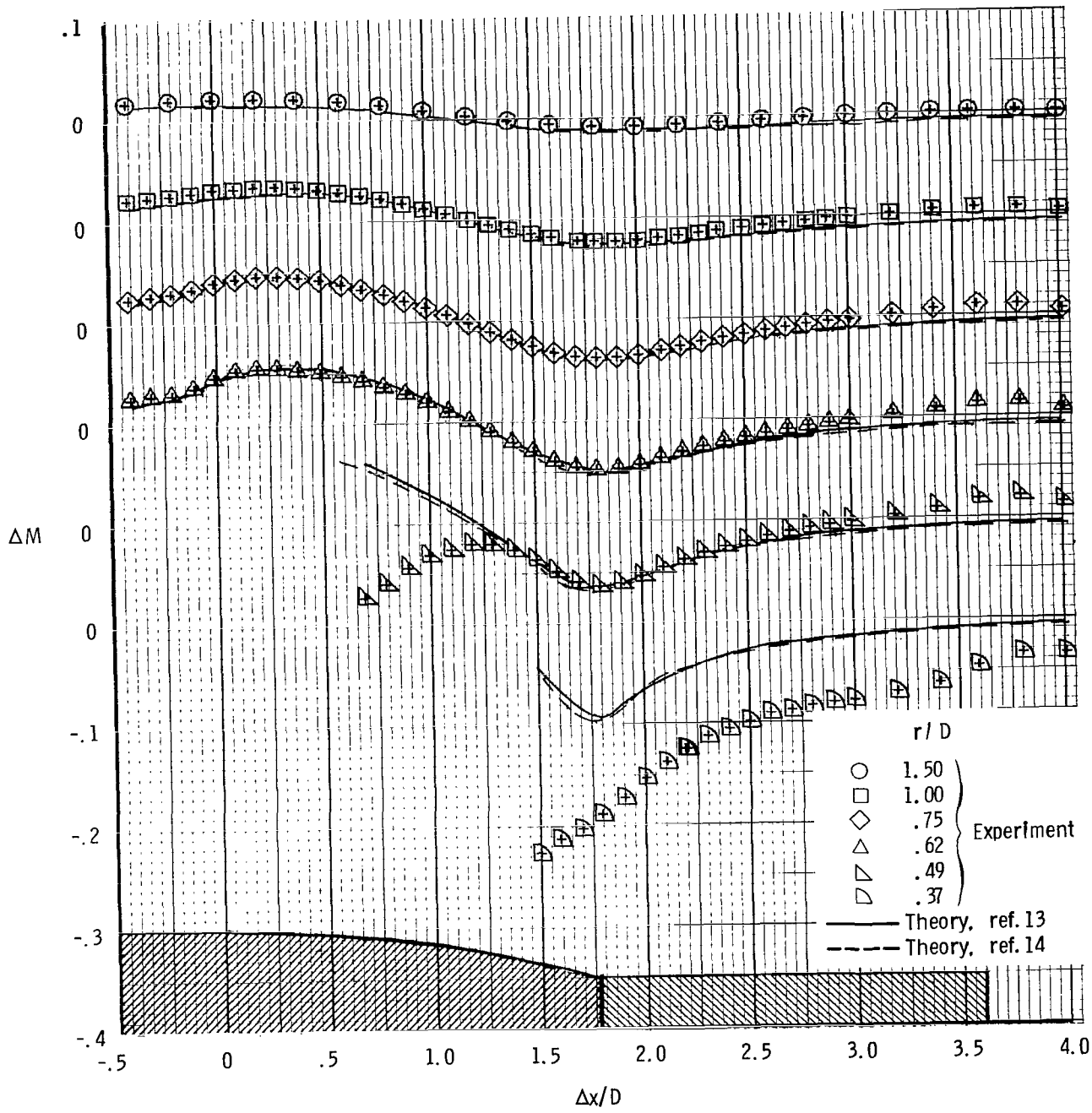

(a) Mach number.

Figure 9.- Flow-field characteristics for $\ell/D = 1.768$ nozzle with solid plume simulator at $M_\infty = 0.80$.

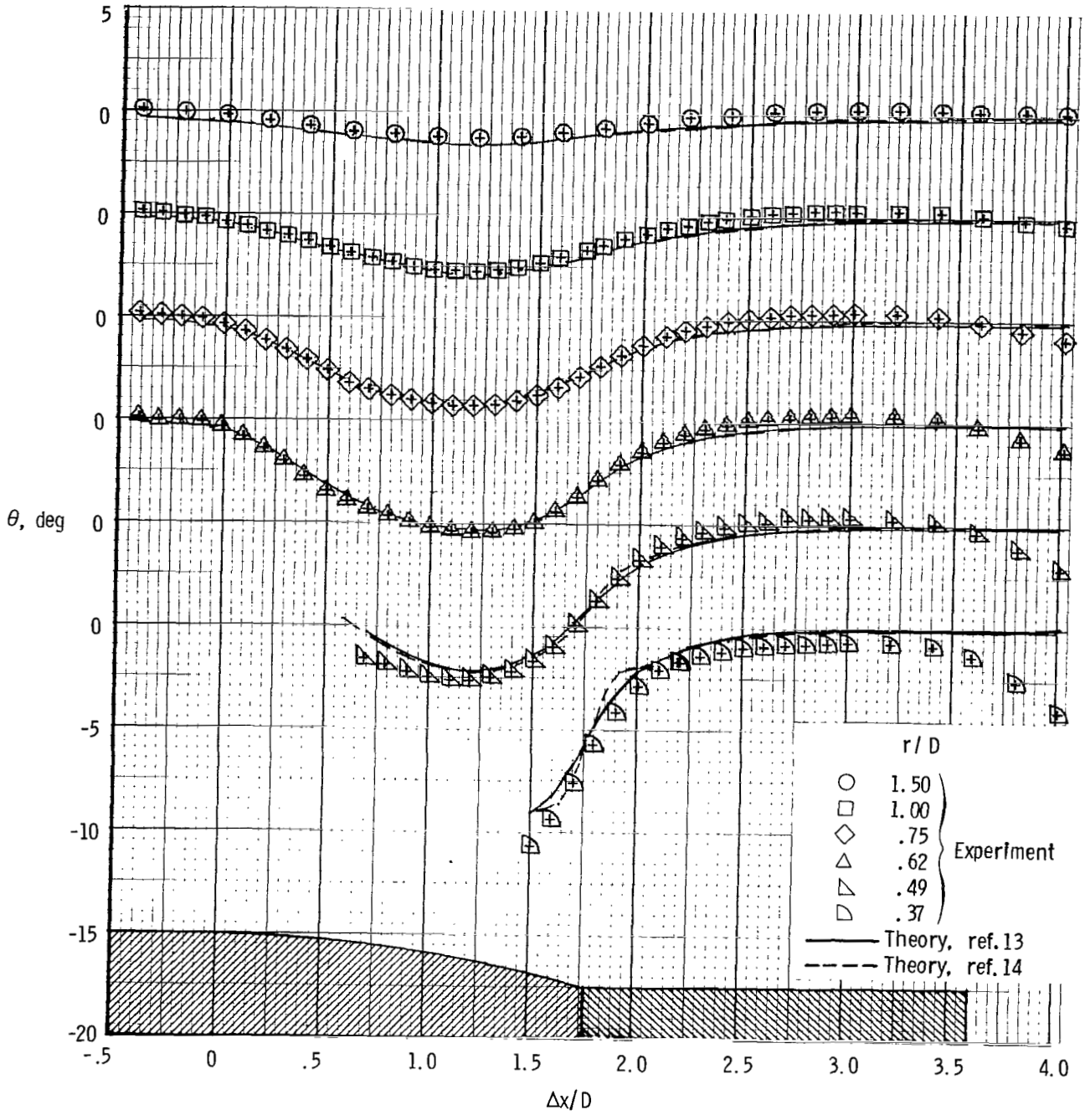

(b) Flow angle.

Figure 9.- Concluded.

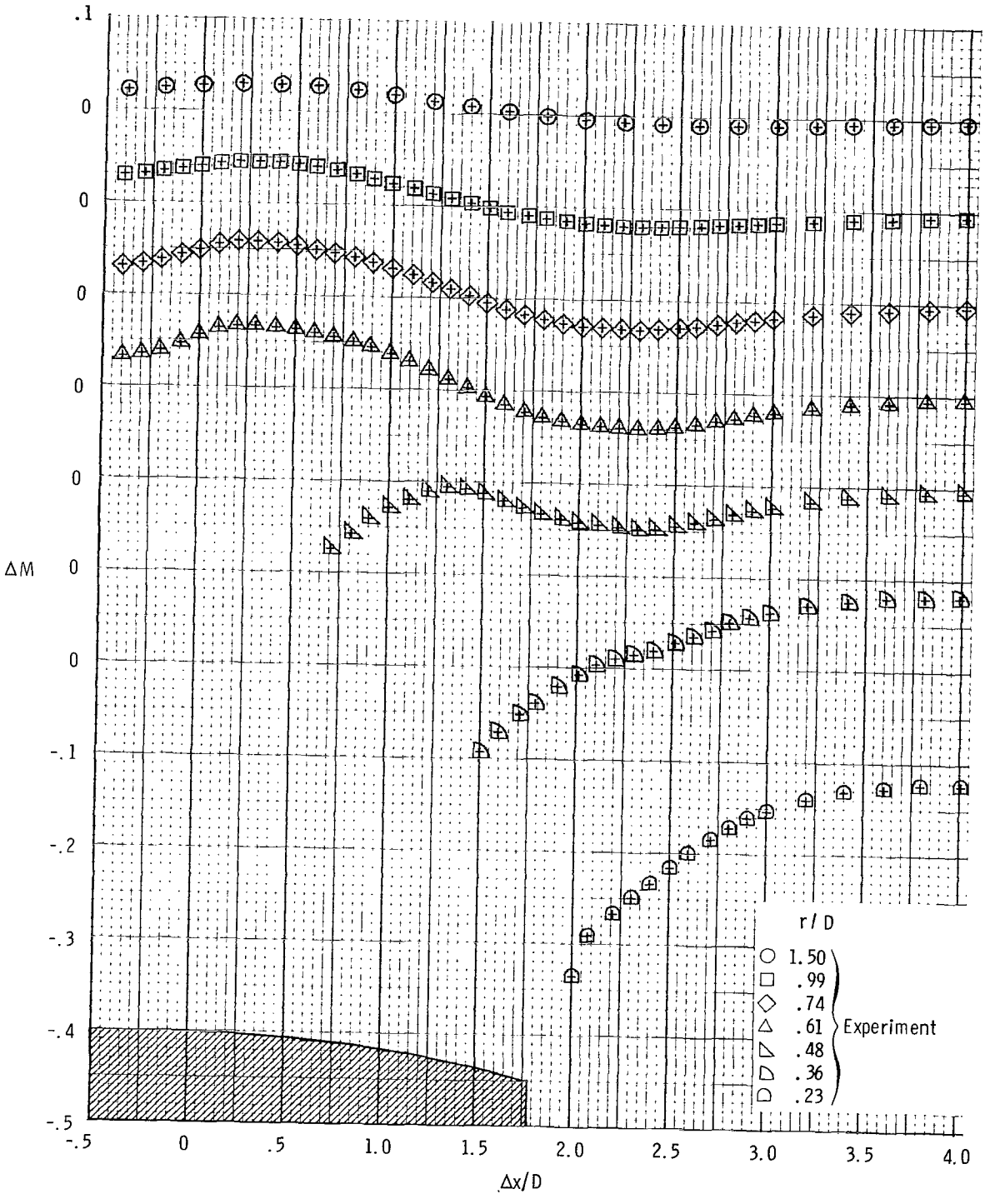

(a) Mach number.

Figure 10.- Flow-field characteristics for $\ell/D = 1.768$ nozzle with jet off and $M_\infty = 0.80$.

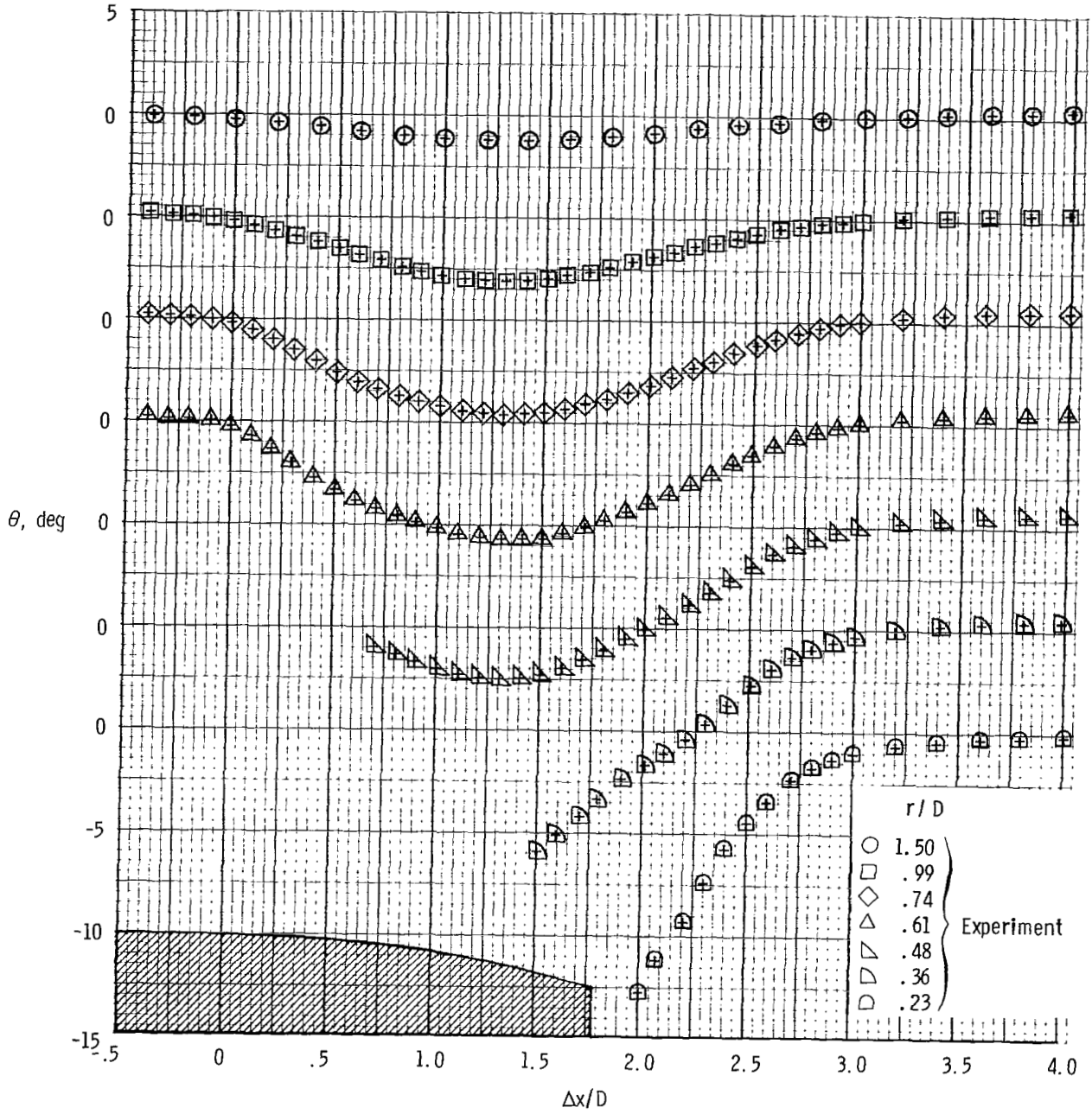

(b) Flow angle.

Figure 10.- Concluded.

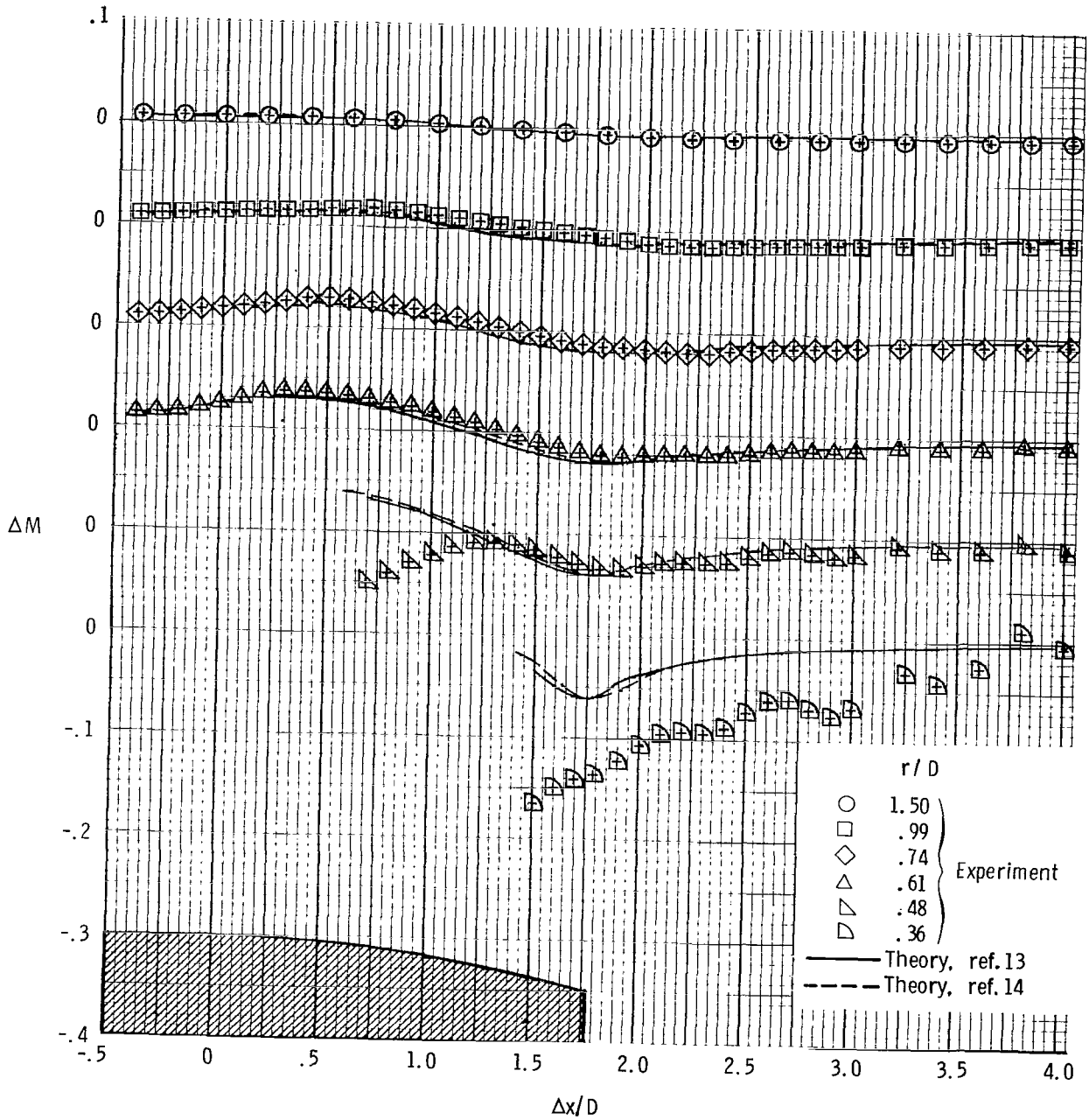

(a) Mach number.

Figure 11.- Flow-field characteristics for l/D = 1.768 nozzle with NPR = 2.9 and M_∞ = 0.60.

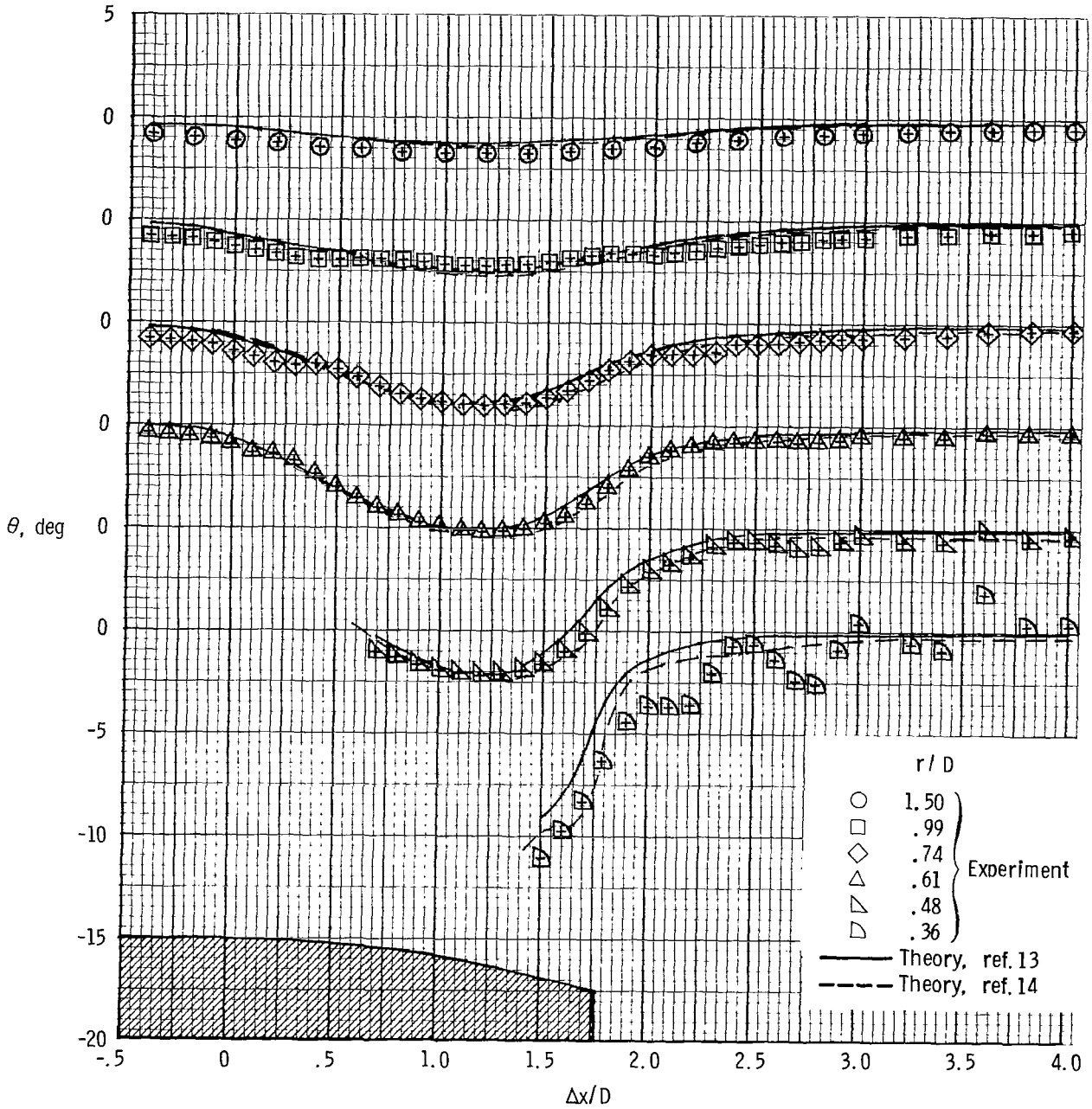

(b) Flow angle.

Figure 11.- Concluded.

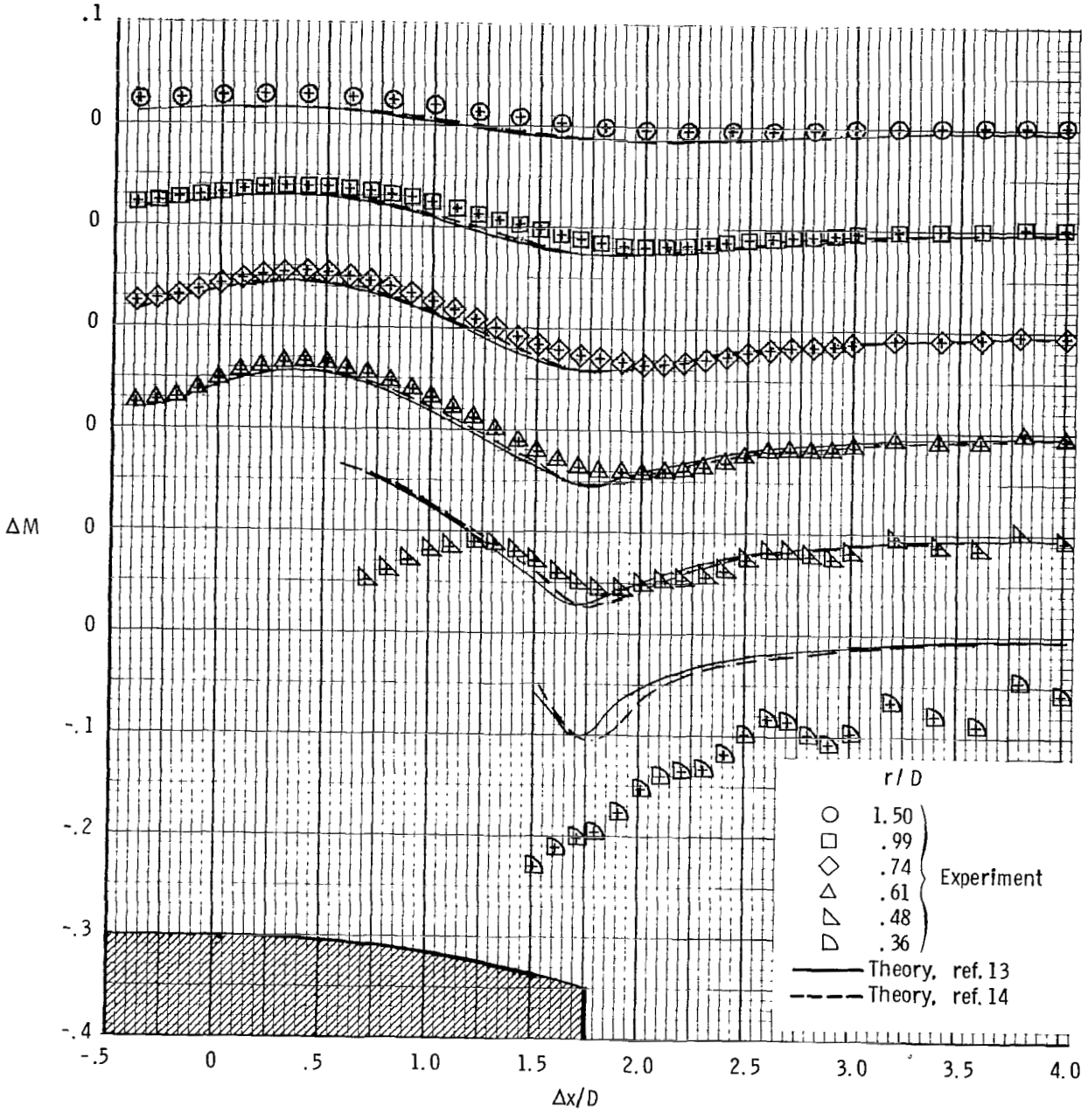

(a) Mach number.

Figure 12.- Flow-field characteristics for $\ell/D = 1.768$ nozzle with NPR = 2.9 and $M_\infty = 0.80$.

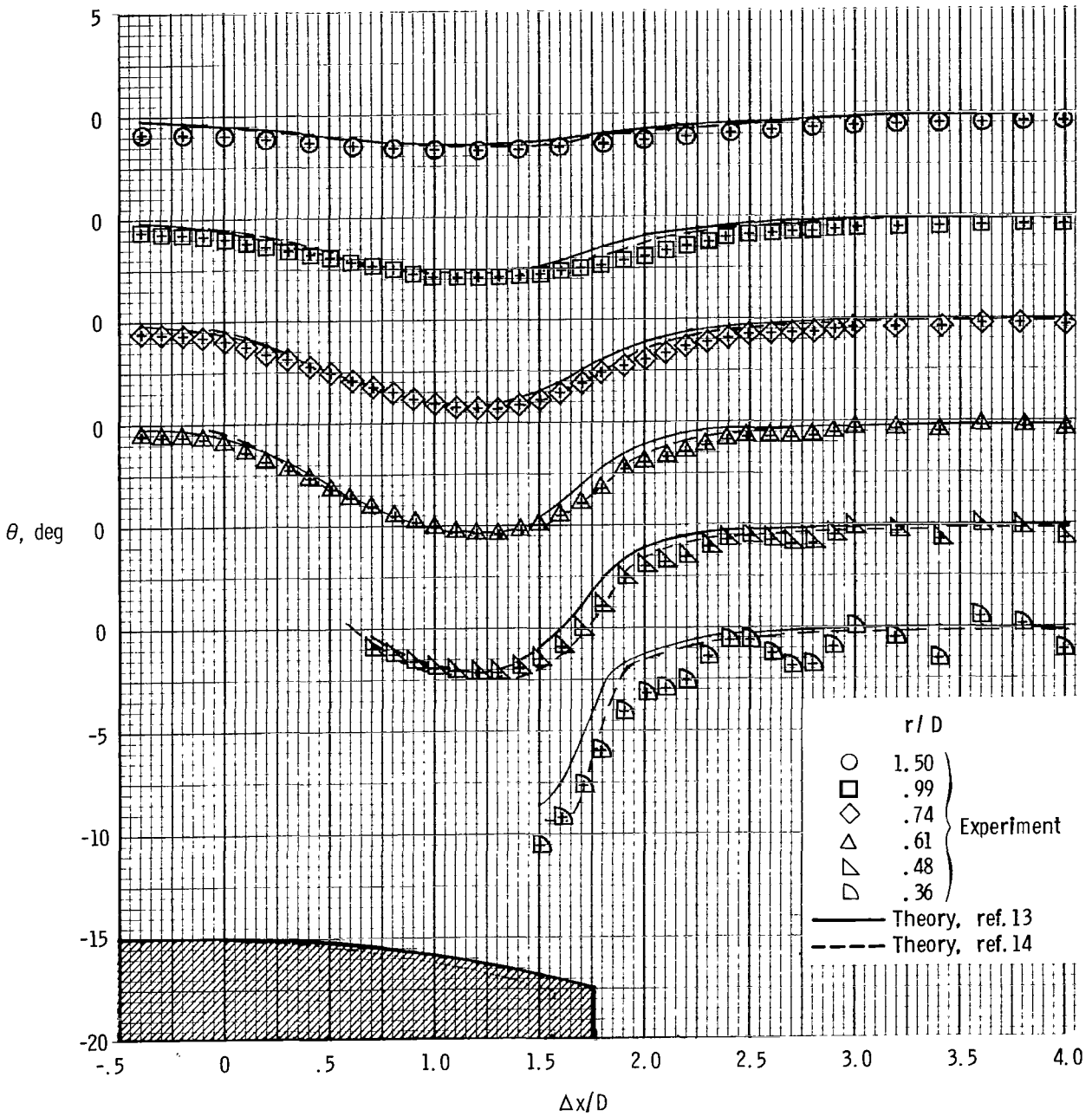

(b) Flow angle.

Figure 12.- Concluded.

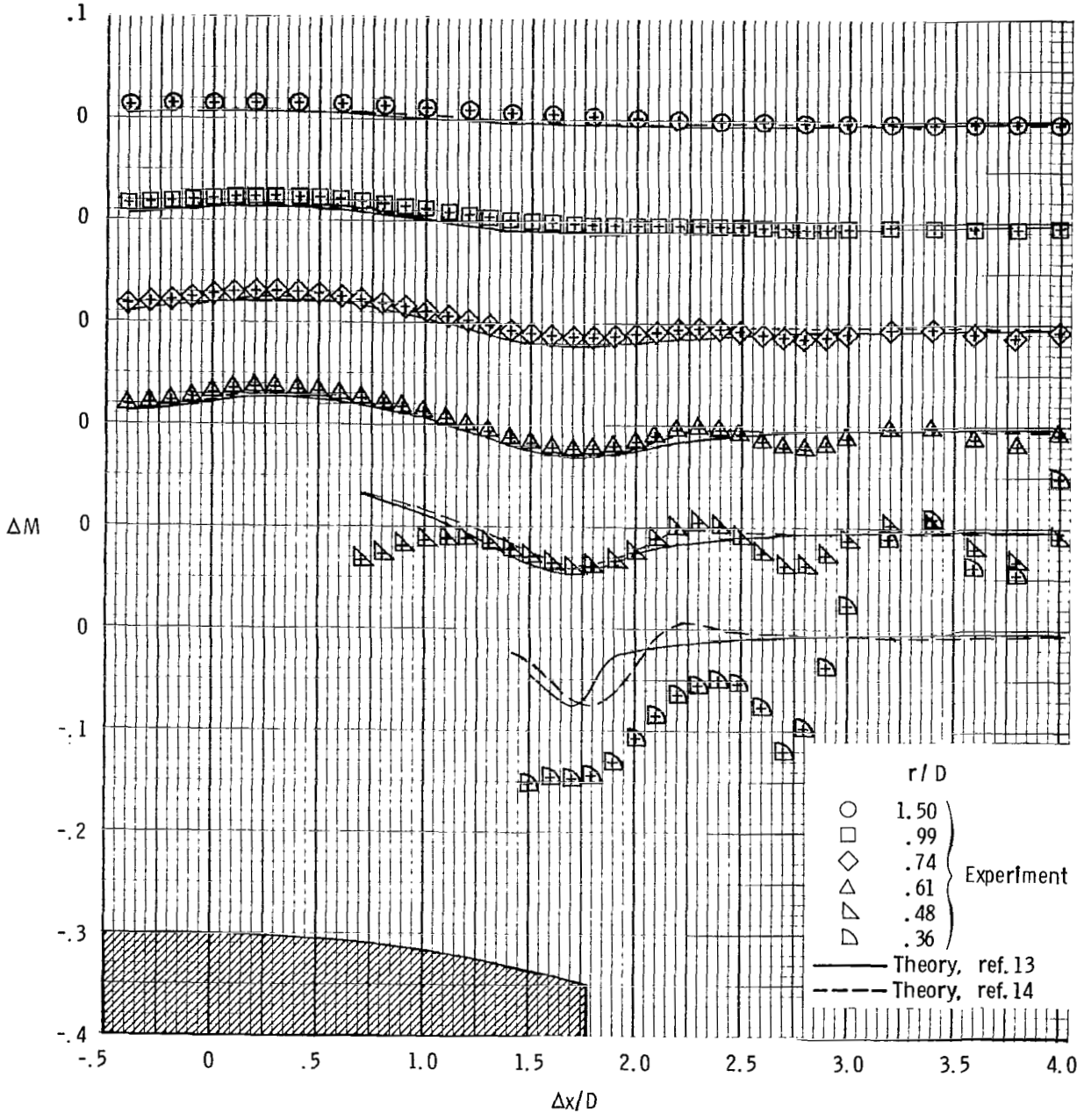

(a) Mach number.

Figure 13.- Flow-field characteristics for $\ell/D = 1.768$ nozzle with NPR = 5.0 and $M_\infty = 0.60$.

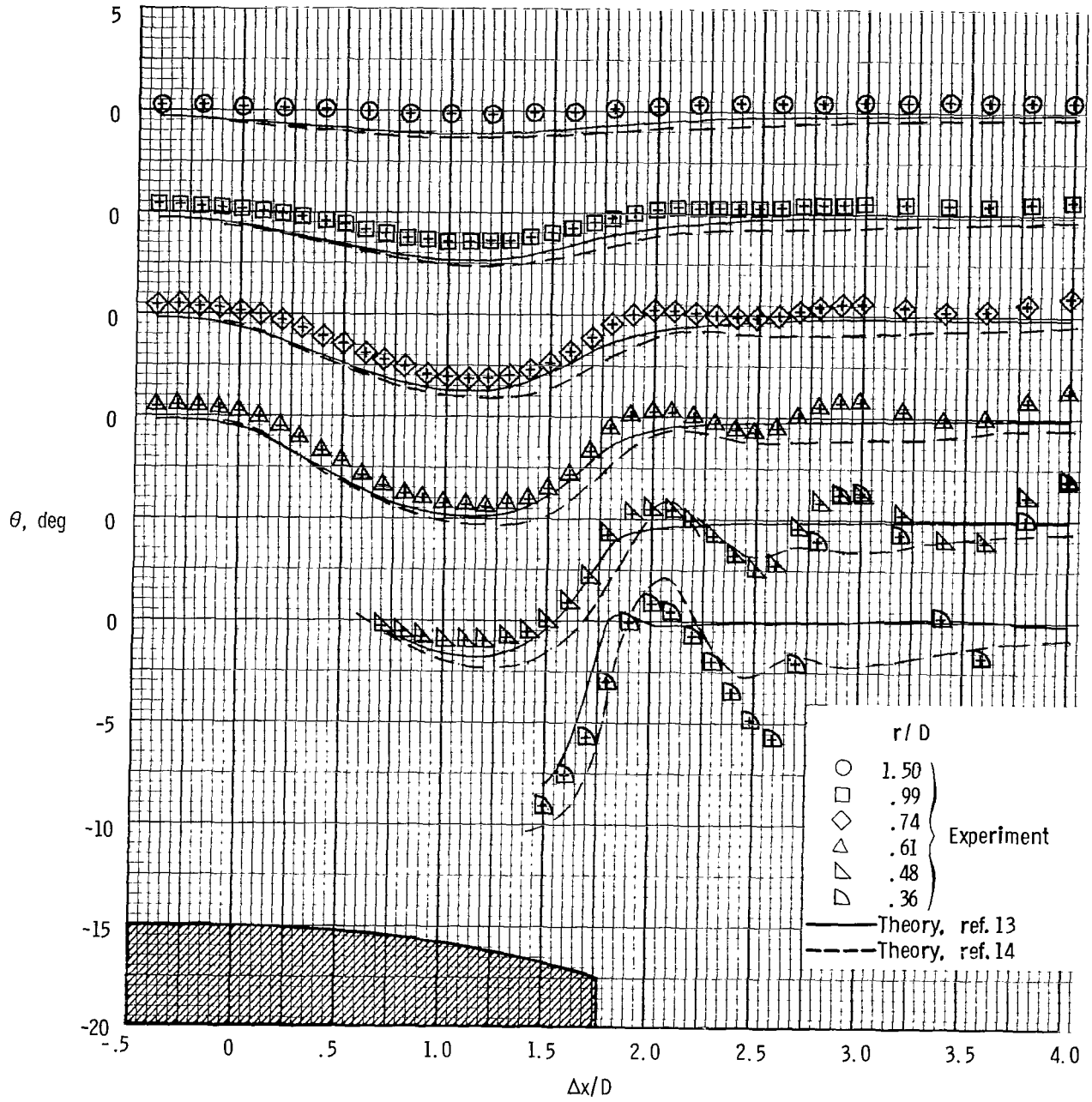

(b) Flow angle.

Figure 13.- Concluded.

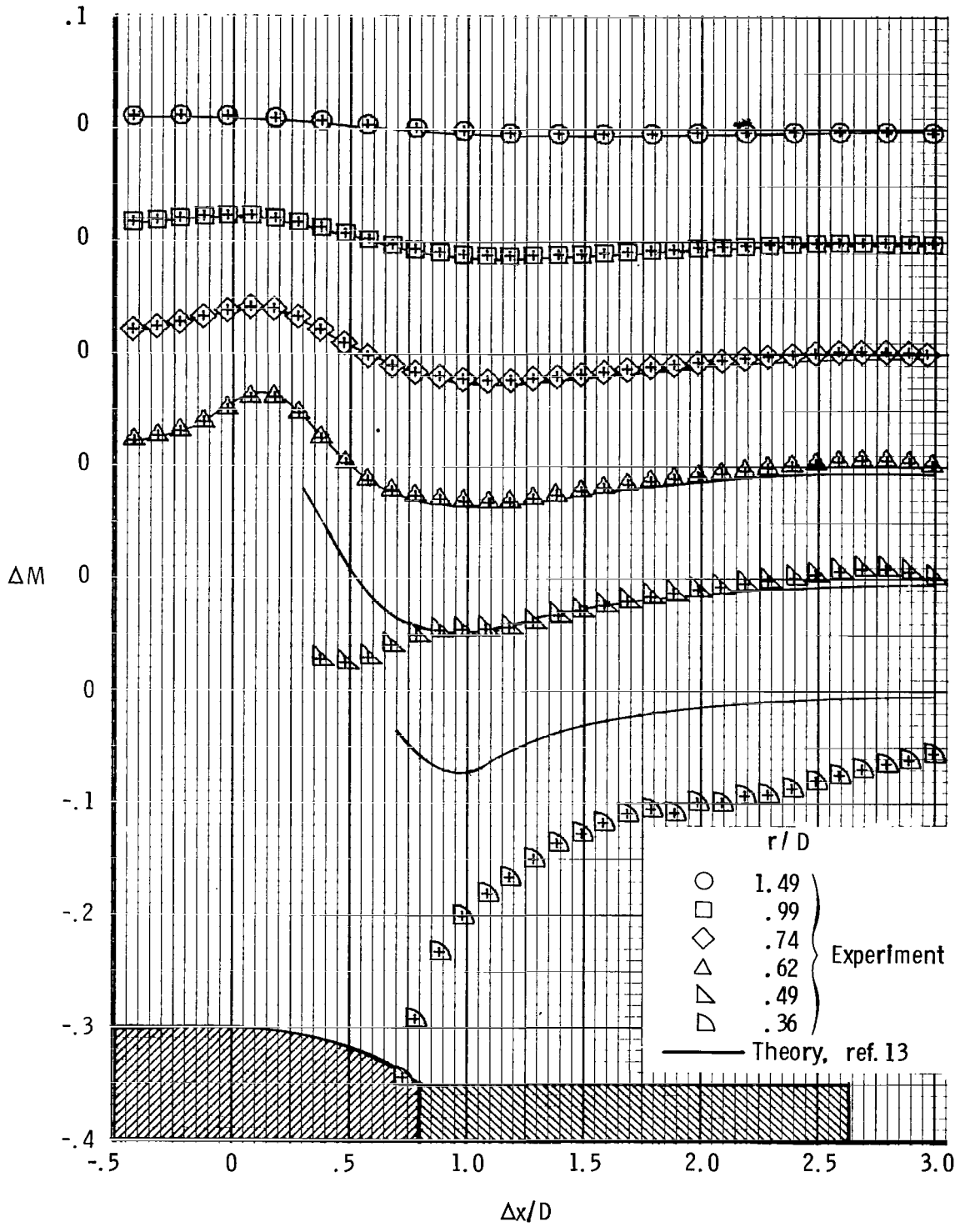

(a) Mach number.

Figure 14.- Flow-field characteristics for $\ell/D = 0.80$ nozzle with solid plume simulator at $M_\infty = 0.60$.

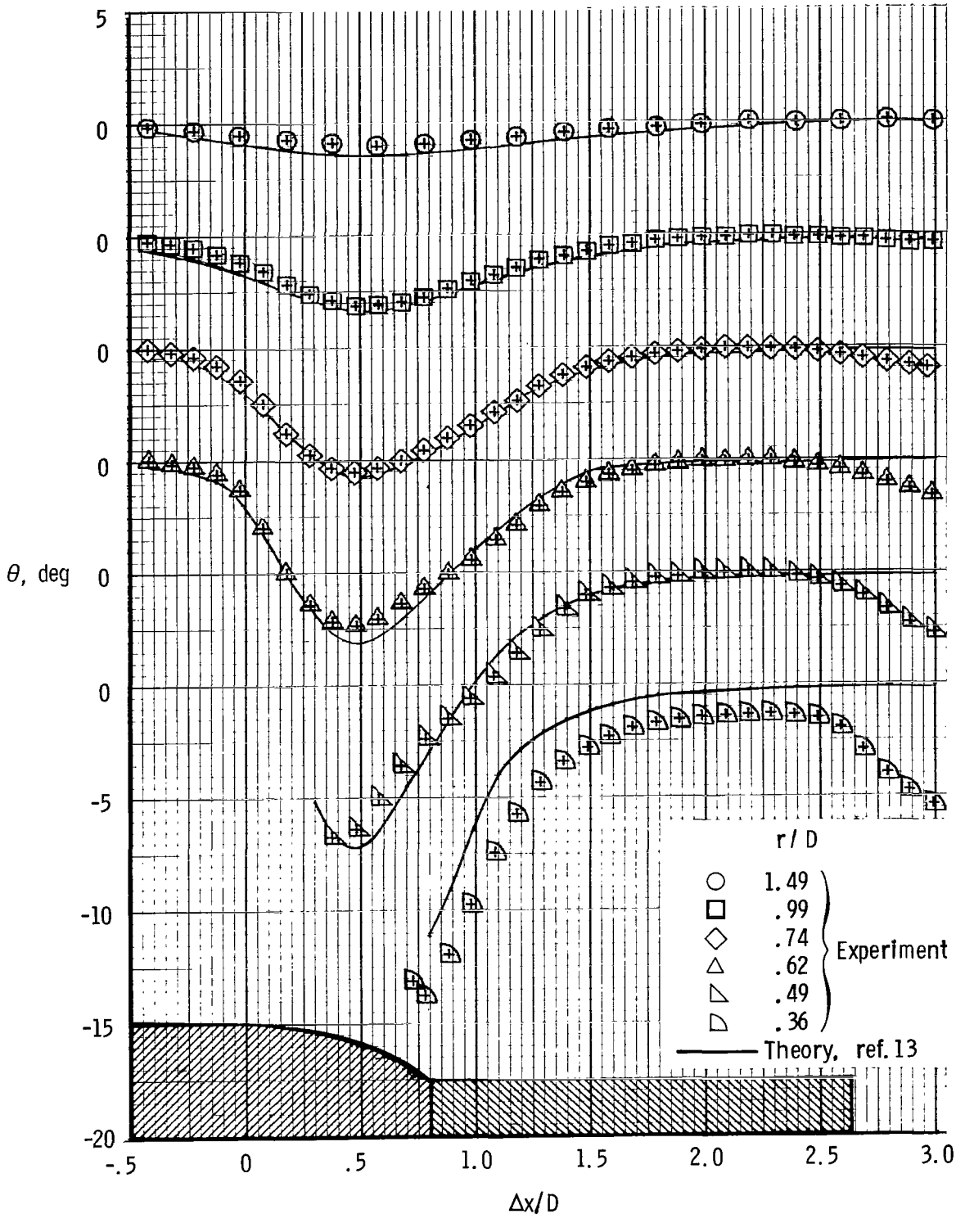

(b) Flow angle.

Figure 14.- Concluded.

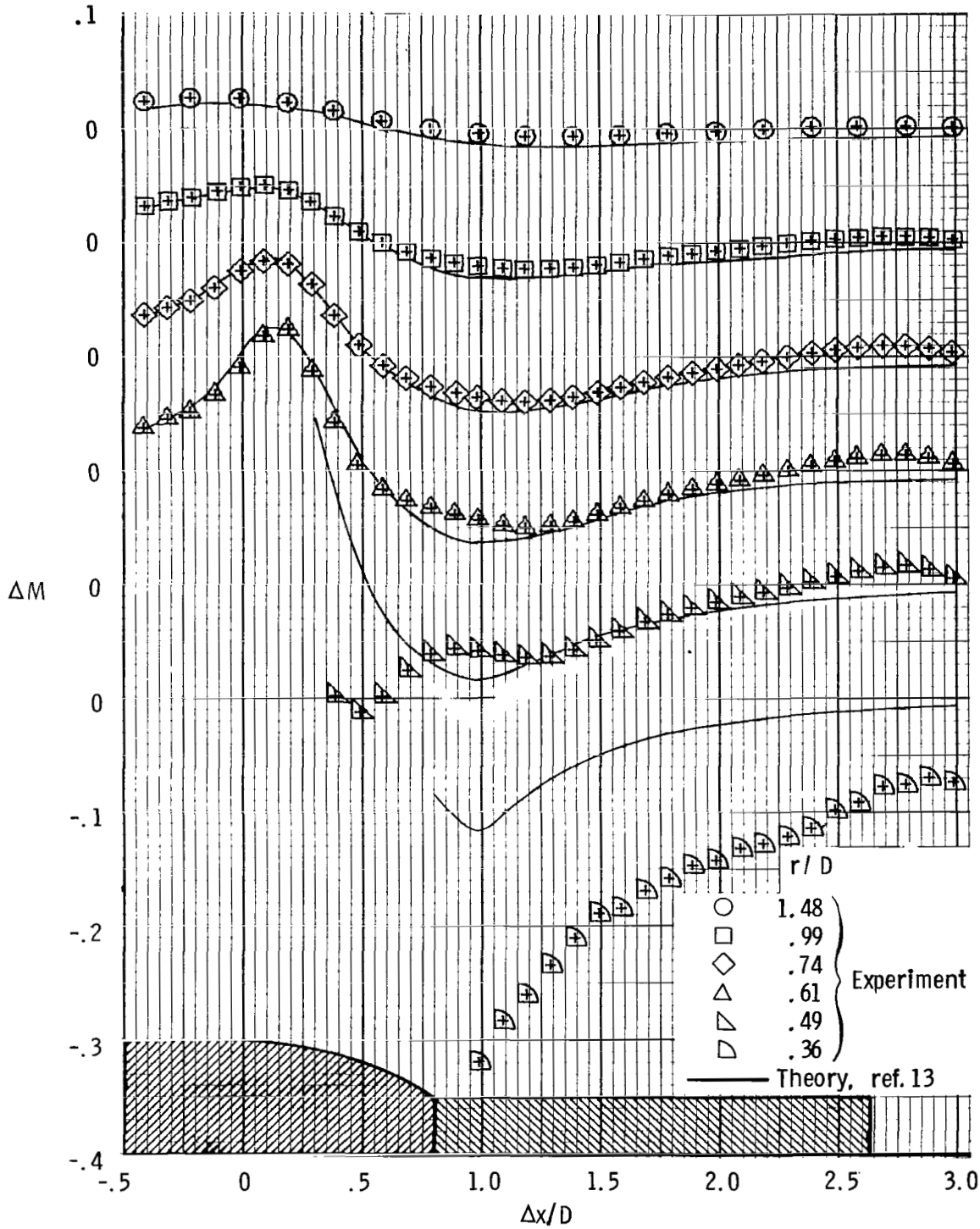

(a) Mach number.

Figure 15.- Flow-field characteristics for $\ell/D = 0.80$ nozzle with solid plume simulator at $M_\infty = 0.80$.

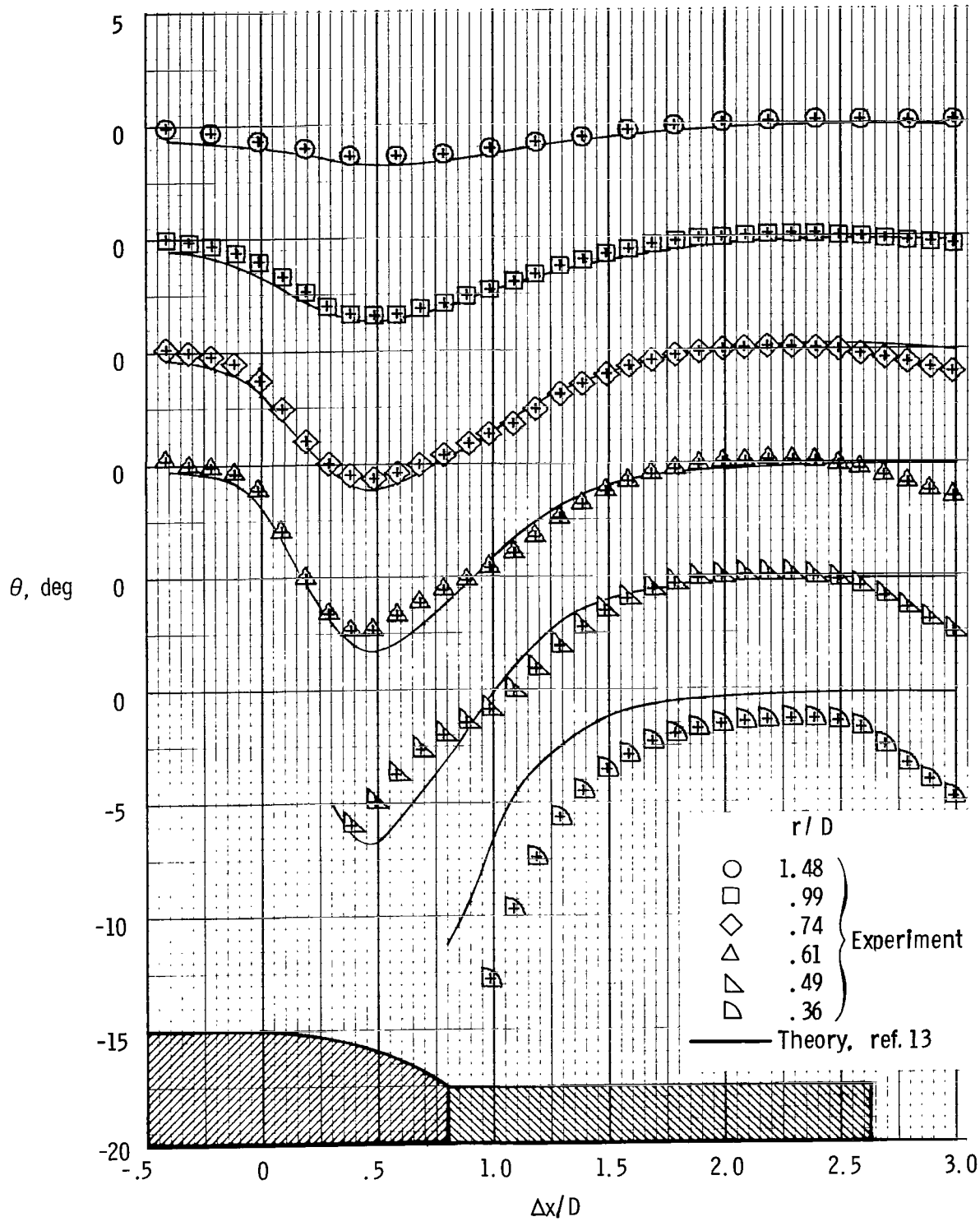

(b) Flow angle.

Figure 15.- Concluded.

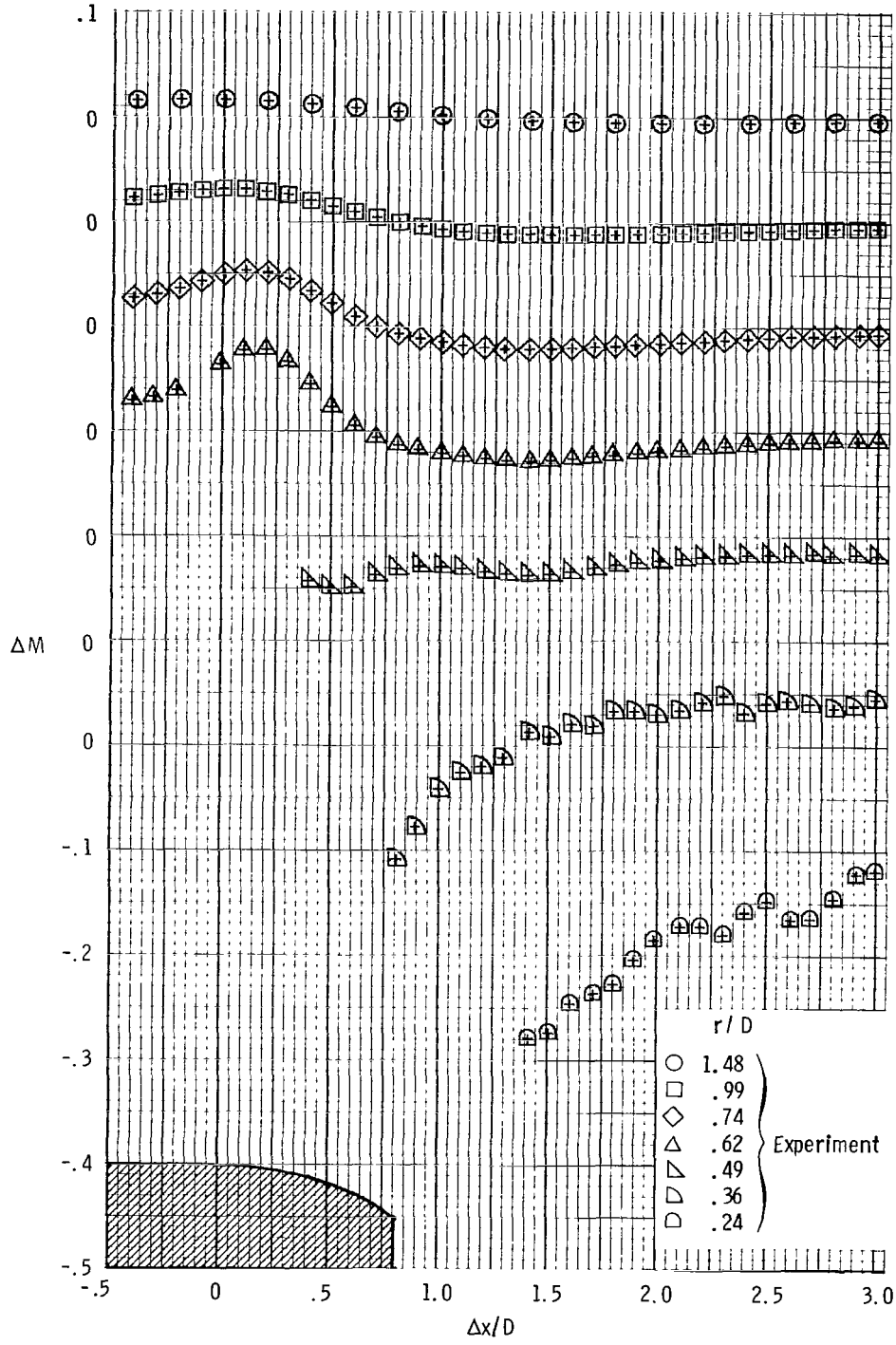

(a) Mach number.

Figure 16.- Flow-field characteristics for $\ell/D = 0.80$ nozzle with jet off and $M_\infty = 0.60$.

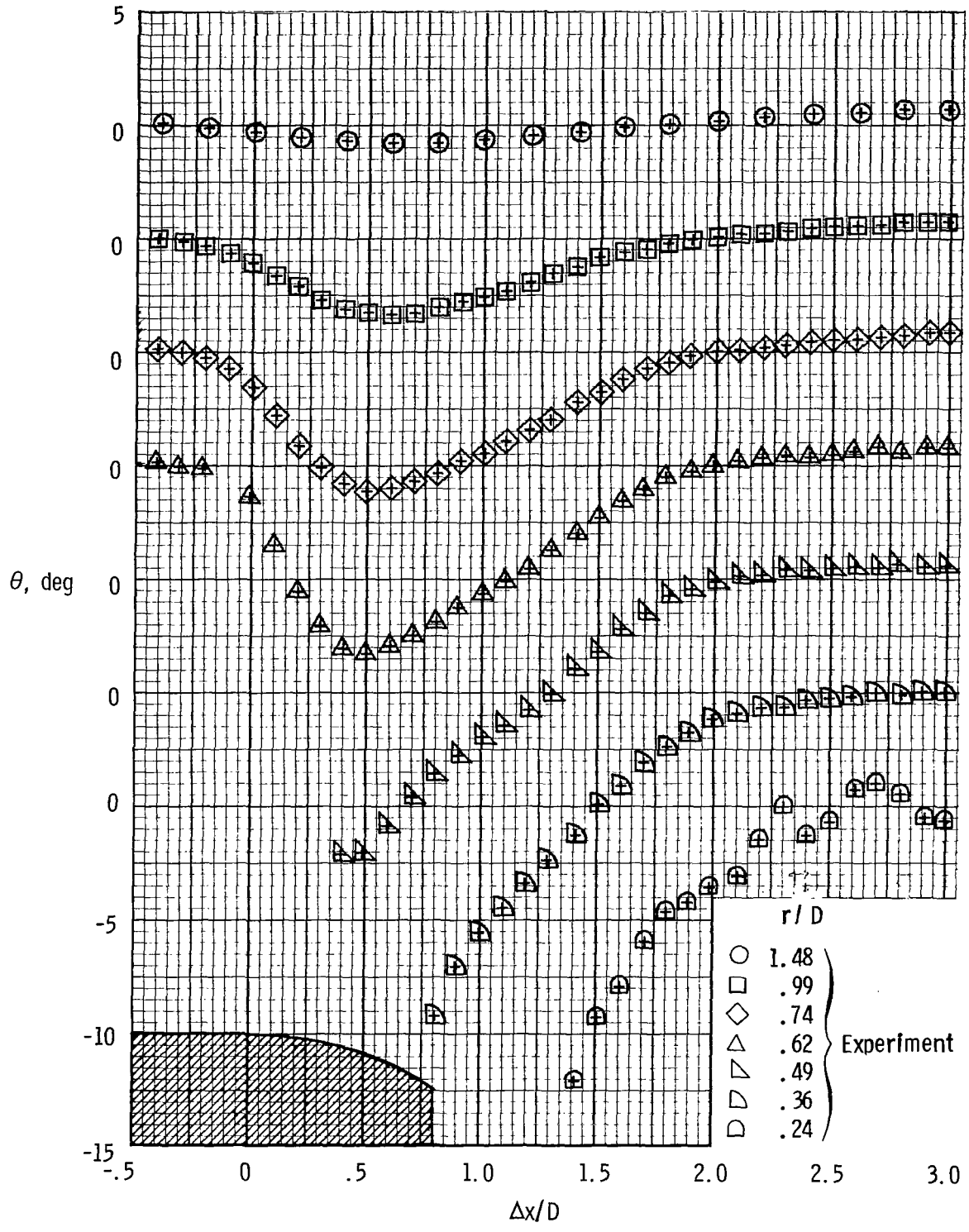

(b) Flow angle.

Figure 16.- Concluded.

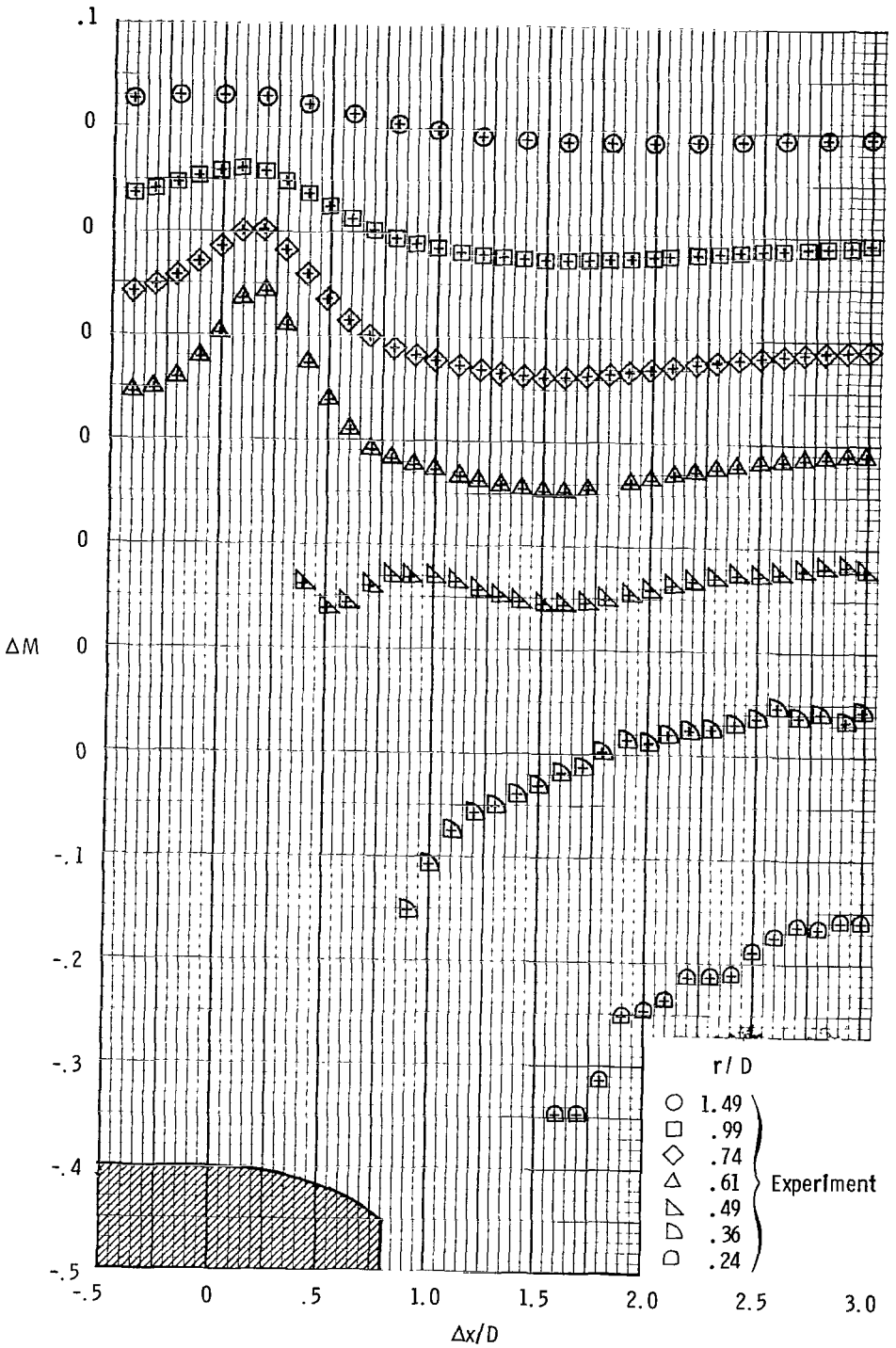

(a) Mach number.

Figure 17.- Flow-field characteristics for $l/D = 0.80$ nozzle with jet off and $M_\infty = 0.80$.

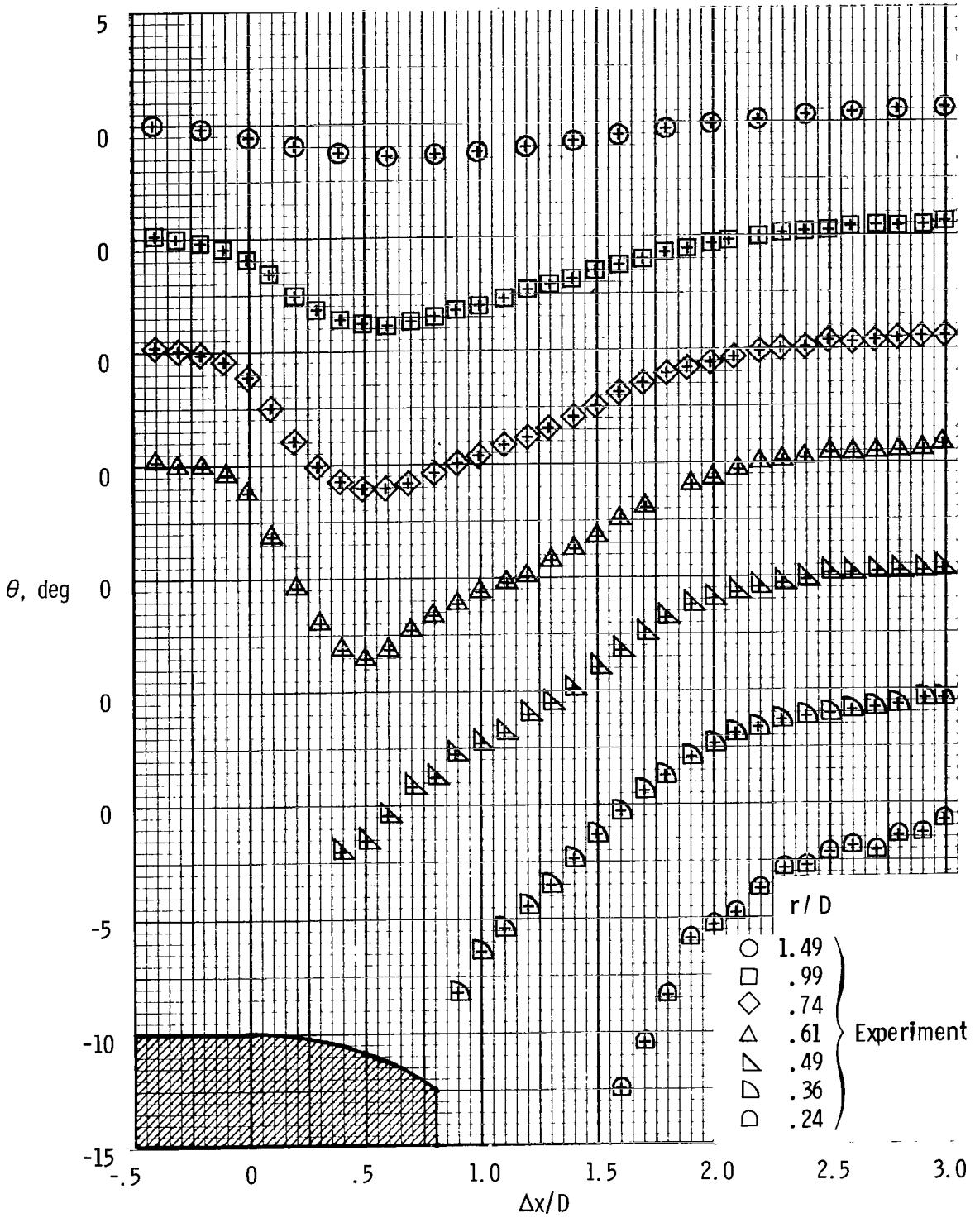

(b) Flow angle.

Figure 17.- Concluded.

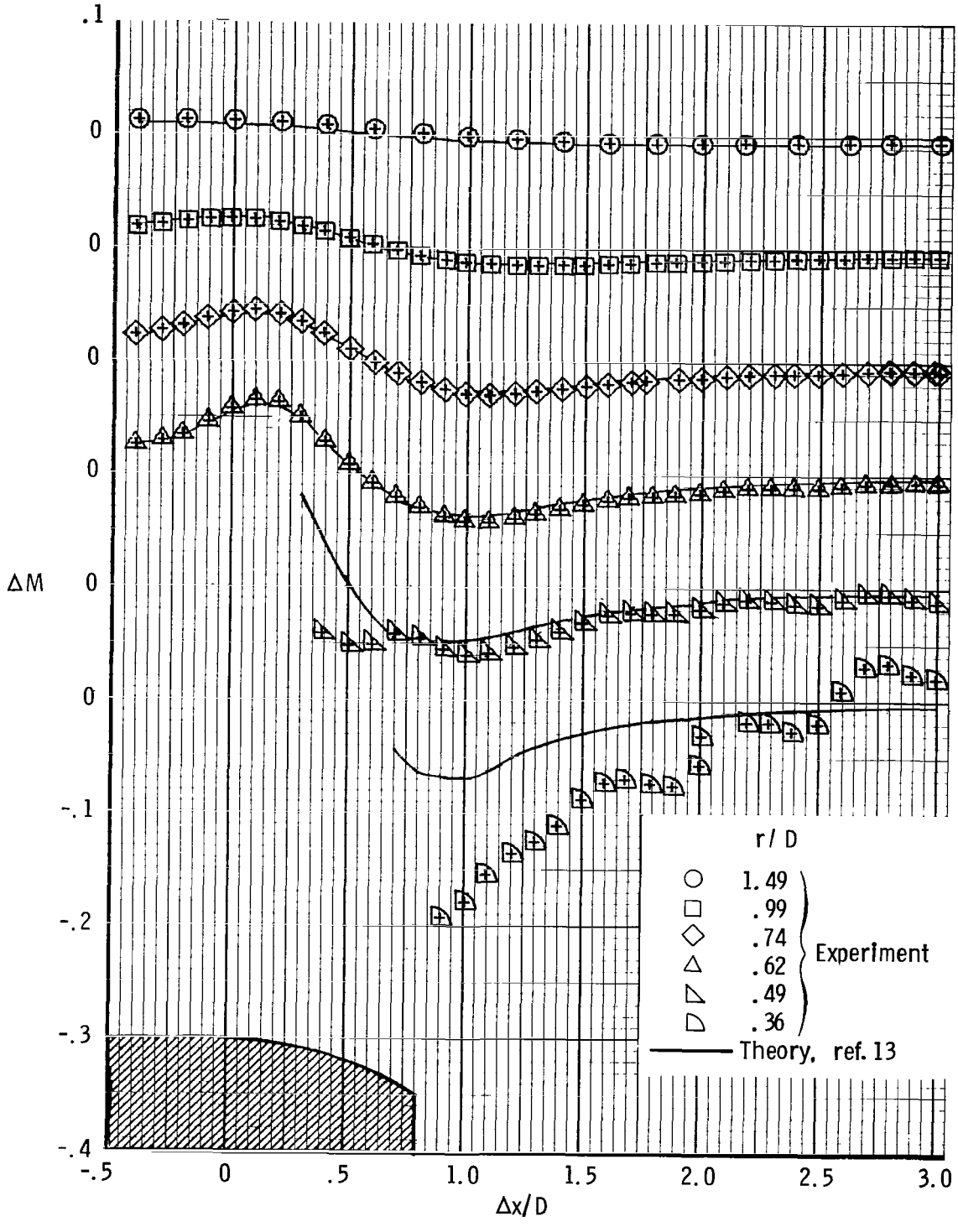

(a) Mach number.

Figure 18.- Flow-field characteristics for $\ell/D = 0.80$ nozzle with NPR = 2.9 and $M_\infty = 0.60$.

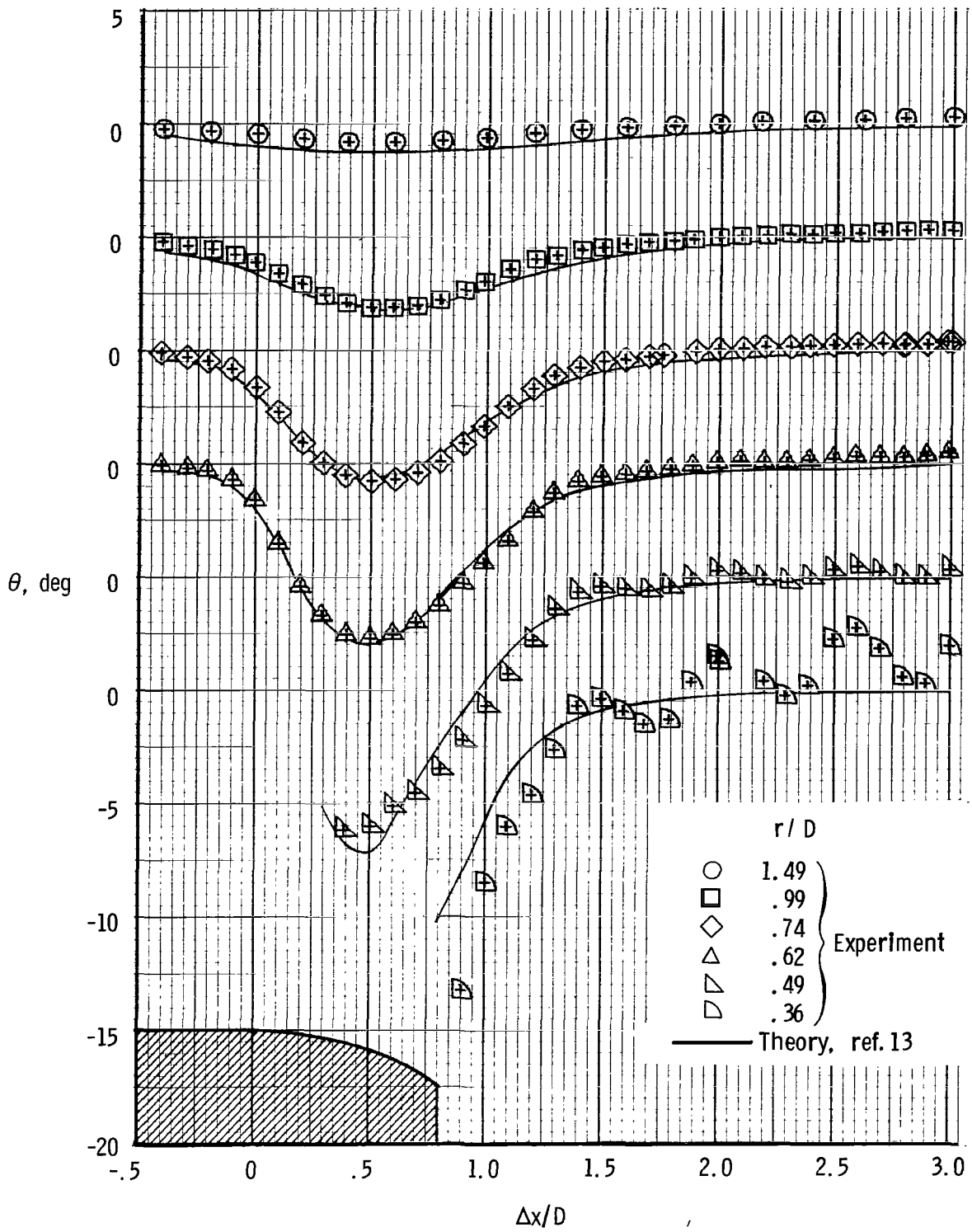

(b) Flow angle.

Figure 18.- Concluded.

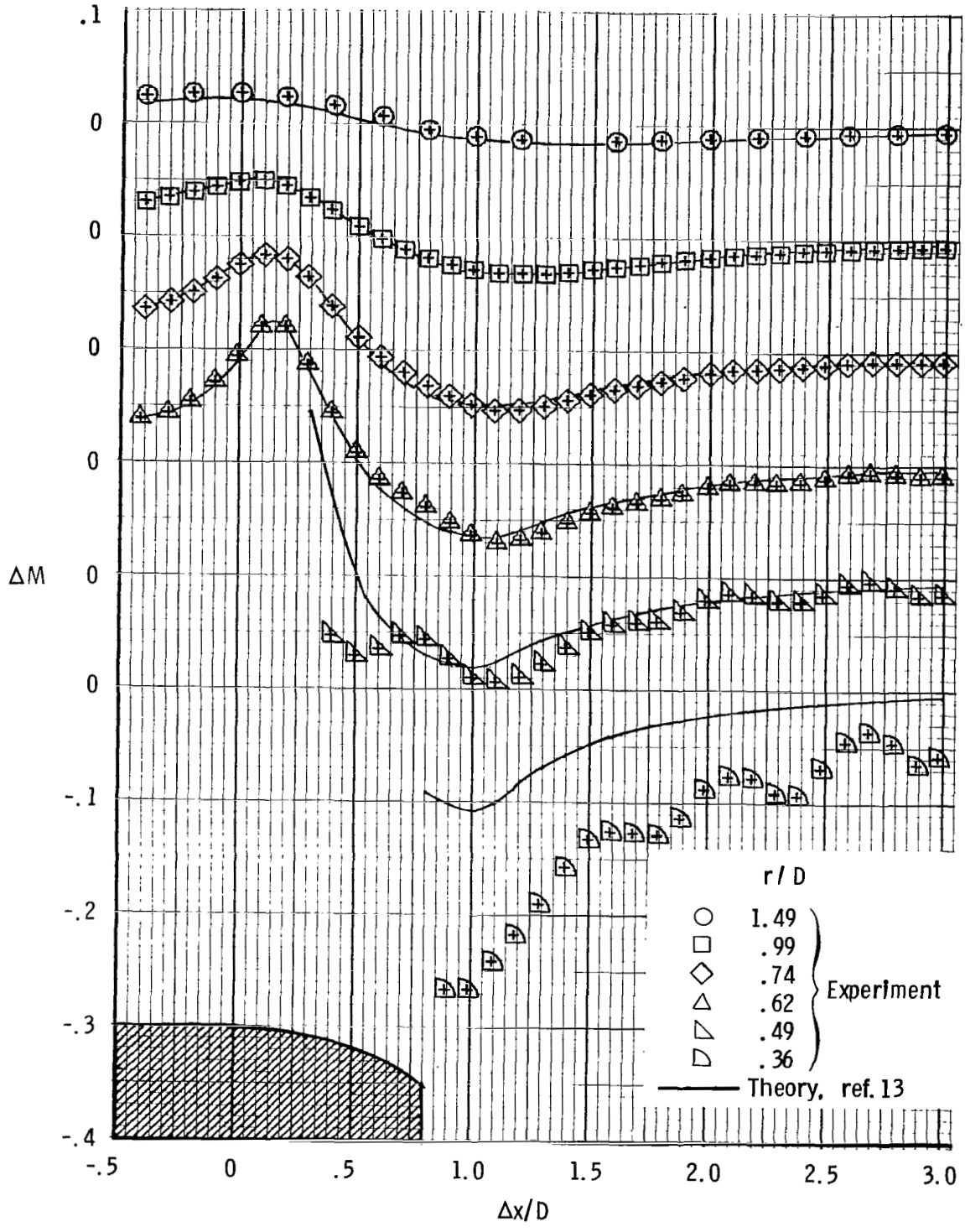

(a) Mach number.

Figure 19.- Flow-field characteristics for $\ell/D = 0.80$ nozzle with NPR = 2.9 and $M_\infty = 0.80$.

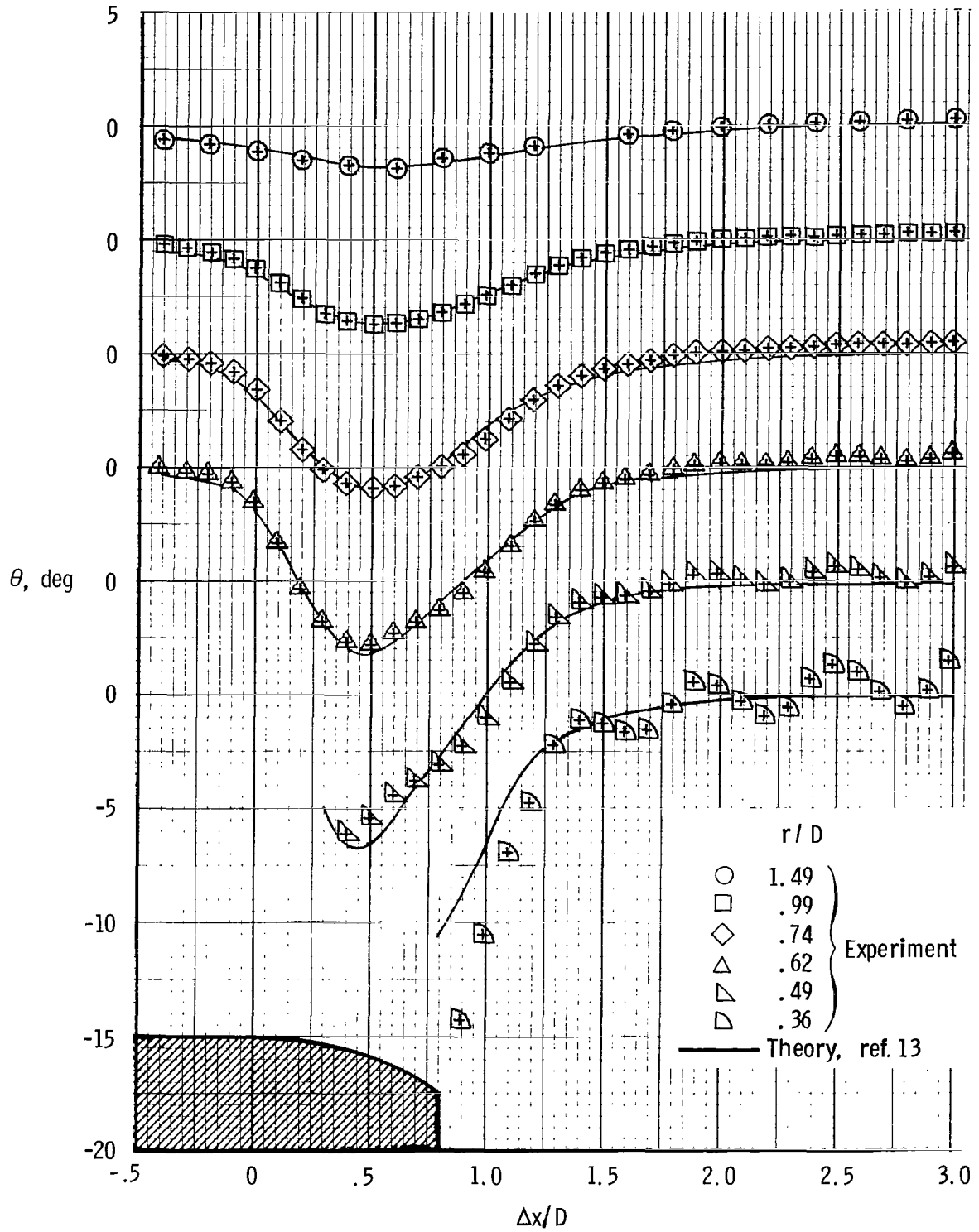

(b) Flow angle.

Figure 19.- Concluded.

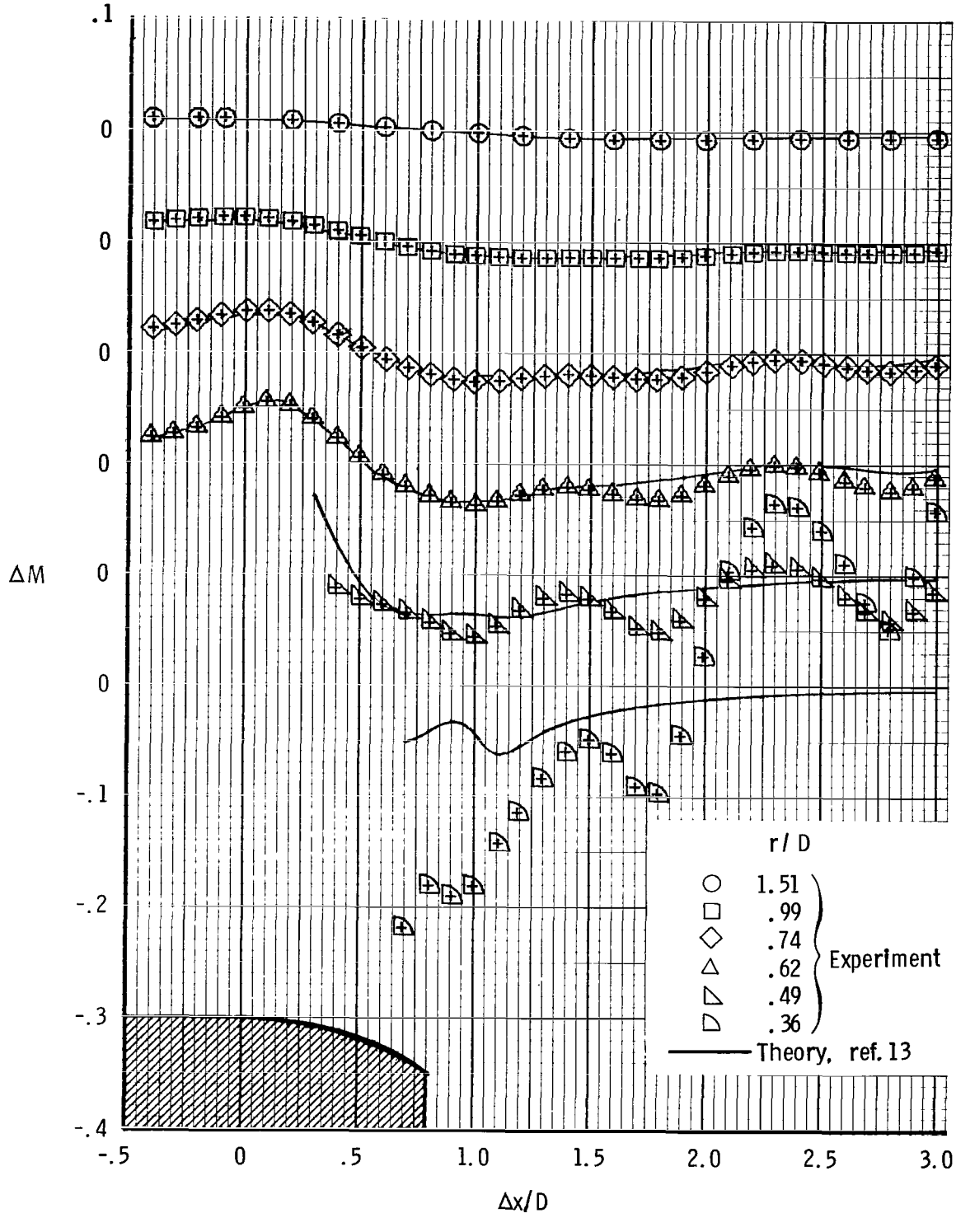

(a) Mach number.

Figure 20.- Flow-field characteristics for $l/D = 0.80$ nozzle with NPR = 5.0 and $M_\infty = 0.60$.

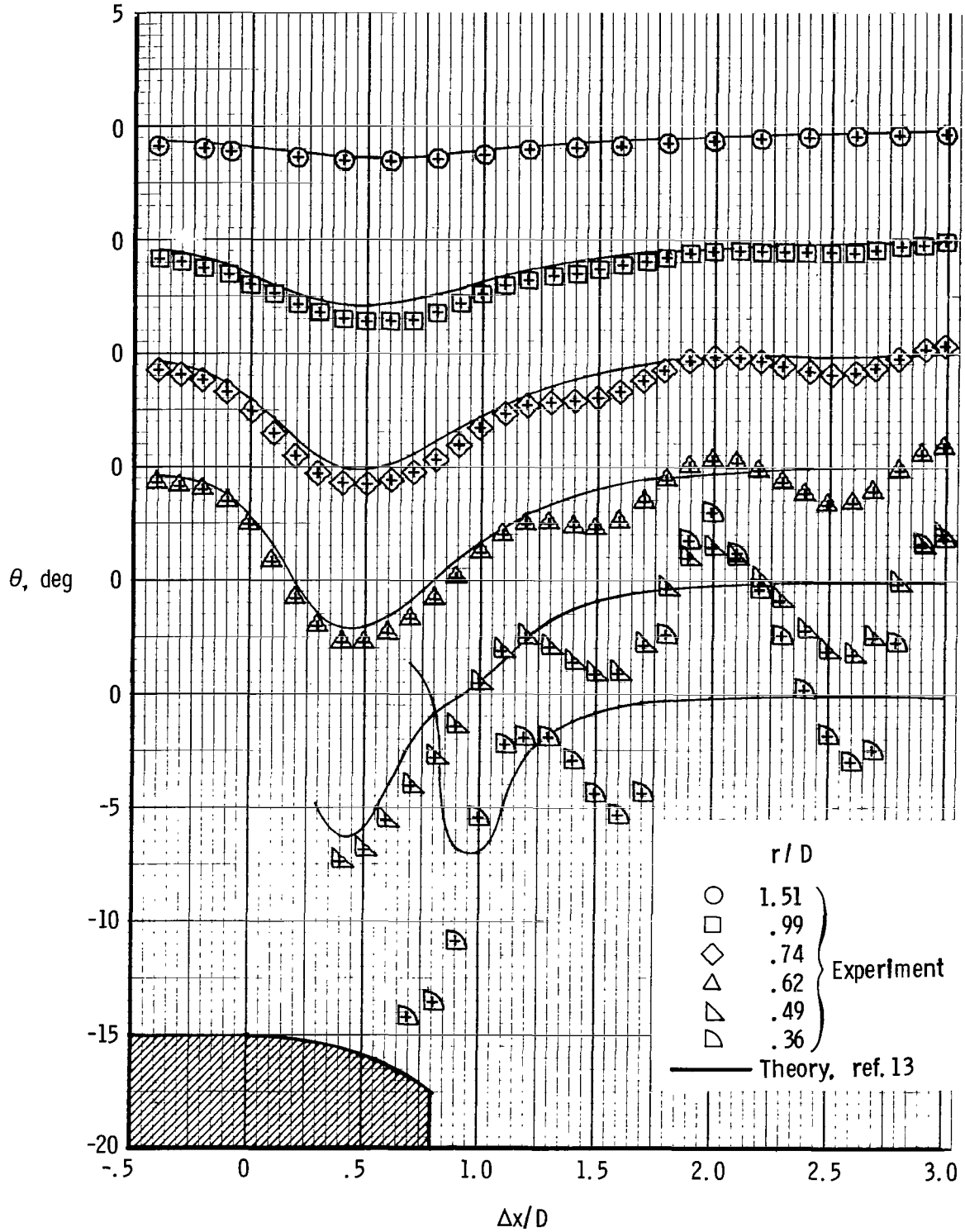

(b) Flow angle.

Figure 20.- Concluded.

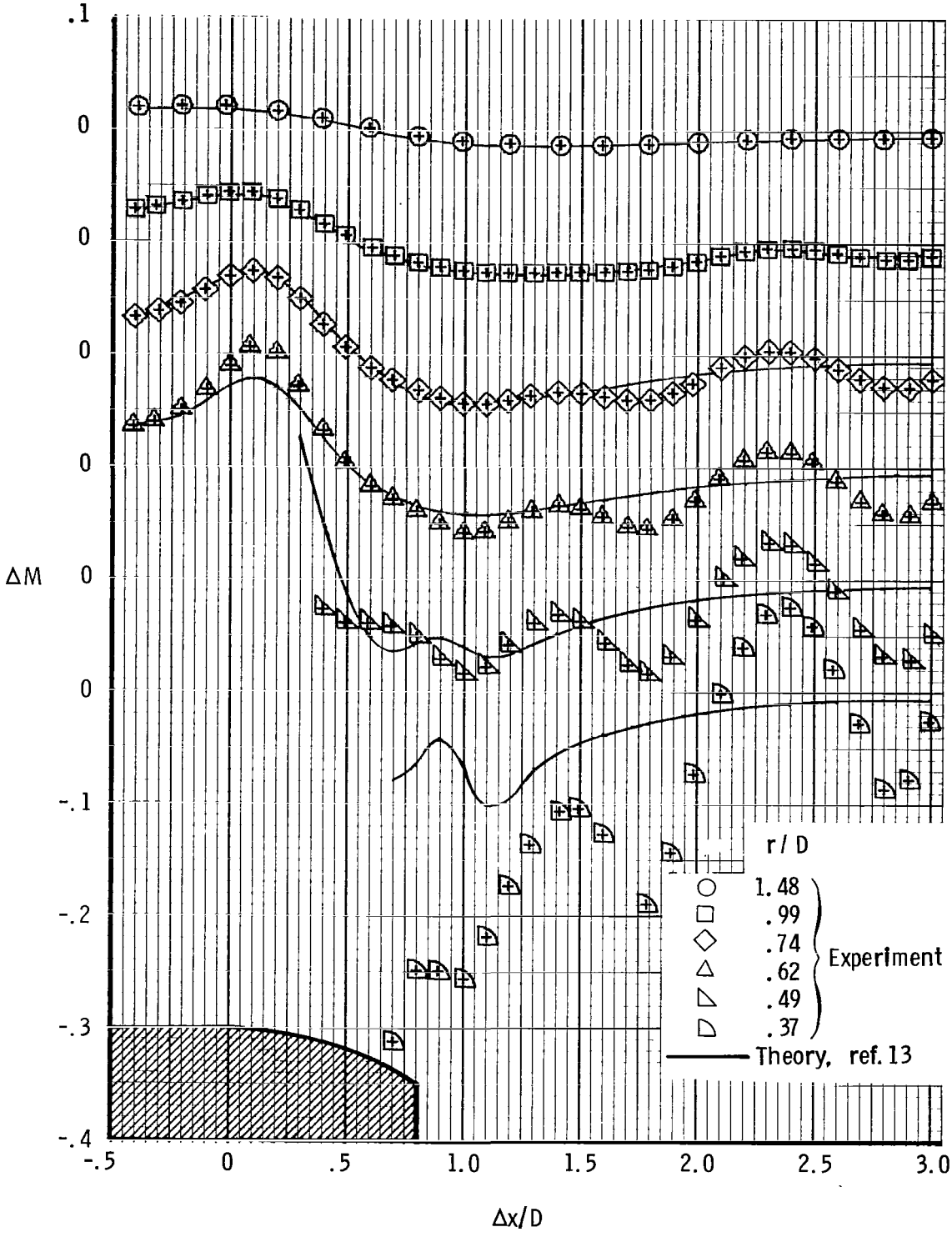

(a) Mach number.

Figure 21.- Flow-field characteristics for $\ell/D = 0.80$ nozzle with NPR = 5.0 and $M_\infty = 0.80$.

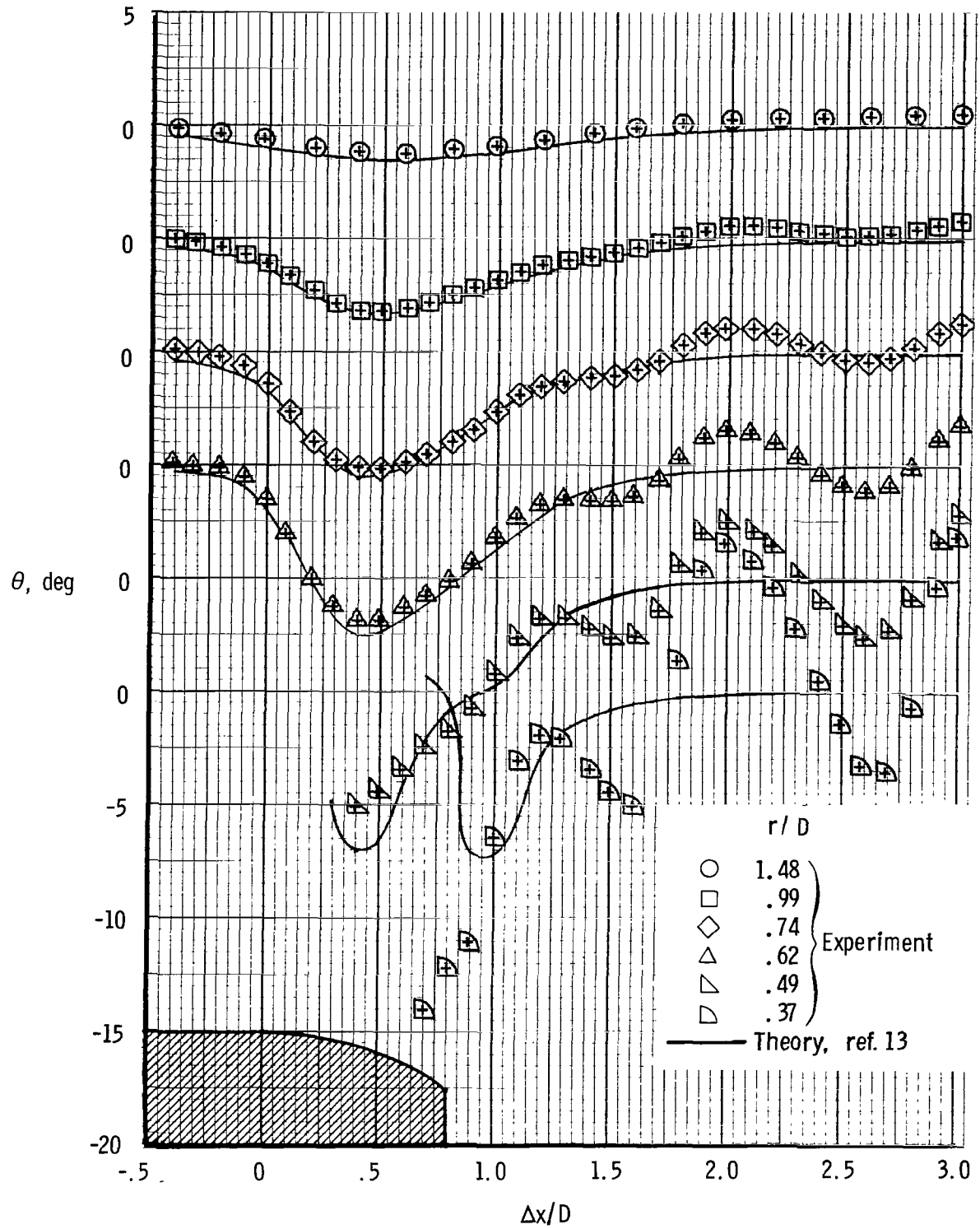

(b) Flow angle.

Figure 21.- Concluded.

1. Report No.	2. Government Accession No.	3. Recipient's Catalog No.
NASA TP-1633		

4. Title and Subtitle	5. Report Date
INVESTIGATION OF THE FLOW FIELD SURROUNDING CIRCULAR-ARC BOATTAIL NOZZLES AT SUBSONIC SPEEDS	May 1980
	6. Performing Organization Code
7. Author(s)	8. Performing Organization Report No.
William K. Abeyounis and Lawrence E. Putnam	L-13318
	10. Work Unit No.
9. Performing Organization Name and Address	505-32-13-01
NASA Langley Research Center Hampton, VA 23665	11. Contract or Grant No.
	13. Type of Report and Period Covered
12. Sponsoring Agency Name and Address	Technical Paper
National Aeronautics and Space Administration Washington, DC 20546	14. Sponsoring Agency Code

15. Supplementary Notes

16. Abstract

An investigation has been conducted to determine the effects of jet exhaust on the subsonic flow field surrounding boattail nozzles with attached and separated boundary layers. Measurements of local Mach numbers and flow angles were made at free-stream Mach numbers of 0.60 and 0.80 at an angle of attack of 0°. Jet-exhaust flow was simulated with a solid cylindrical sting and with high-pressure air at jet-nozzle total-pressure ratios of 2.9 and 5.0. Results show strong effects of the jet-wave structure on the external flow field. The predicted local Mach numbers and flow angles for attached-flow nozzles with solid jet simulators obtained by using subsonic inviscid/viscous-flow theory are in good agreement with experimental data. Prediction of nozzle surface-pressure distributions which include jet-entrainment effects also agree with experimental data for attached-flow nozzles with high-pressure air jets.

17. Key Words (Suggested by Author(s))	18. Distribution Statement
Nozzle Boattail Flow field Jet entrainment	Unclassified - Unlimited Subject Category 02

19. Security Classif. (of this report)	20. Security Classif. (of this page)	21. No. of Pages	22. Price*
Unclassified	Unclassified	48	$4.50

For sale by the National Technical Information Service, Springfield, Virginia 22161

NASA-Langley, 1980

National Aeronautics and Space Administration

Washington, D.C.
20546

Official Business
Penalty for Private Use, $300

THIRD-CLASS BULK RATE

Postage and Fees Paid
National Aeronautics and Space Administration
NASA-451

U.S.MAIL

2 1 1U,A, 041480 S00903DS
DEPT OF THE AIR FORCE
AF WEAPONS LABORATORY
ATTN: TECHNICAL LIBRARY (SUL)
KIRTLAND AFB NM 87117

NASA

POSTMASTER: If Undeliverable (Section 158 Postal Manual) Do Not Return